

The Air–Sea Interaction Profiler (ASIP): An Autonomous Upwardly Rising Profiler for Microstructure Measurements in the Upper Ocean

BRIAN WARD,* TIM FRISTEDT,⁺ ADRIAN H. CALLAGHAN,[#] GRAIG SUTHERLAND,*.[@]
XAVIER SANCHEZ,[&] JÉRÔME VIALARD,** AND ANNEKE TEN DOESCHATE*

* School of Physics, and Ryan Institute, National University of Ireland, Galway, Galway, Ireland

⁺ Swedish Defence Research Agency (FOI), Stockholm, Sweden

[#] Scripps Institution of Oceanography, University of California, San Diego, La Jolla, California

[&] Department of Physics, University of Gerona, Campus Montilivi, Gerona, Catalonia, Spain

** Sorbonne Universités, UPMC, Université Paris 06, CNRS/IRD/MNH, LOCEAN Laboratory, IPSL, Paris, France

(Manuscript received 12 January 2014, in final form 2 July 2014)

ABSTRACT

The upper few meters of the ocean form a critical layer for air–sea interaction, but because of observational challenges this region is undersampled. However, the physical processes controlling momentum transfer, gas exchange, and heat transfer are all concentrated in the uppermost region of the ocean. To study this region, the Air–Sea Interaction Profiler (ASIP) was developed. This is an autonomous microstructure vertical profiling instrument that provides data from a maximum depth of 100 m to the ocean surface and allows measurements to be performed in an undisturbed environment. The core sensor package on ASIP includes shear probes, microstructure and CTD-quality temperature and conductivity sensors, a photosynthetically active radiation (PAR) sensor, and an oxygen optode providing a repeated high-resolution dataset immediately below the air–sea interface. Autonomous profiling is accomplished with thrusters that submerge the positively buoyant instrument. Once the desired depth is reached, ASIP ascends through the water column acquiring data. At the surface, ASIP acquires its position and transmits this over the Iridium satellite network. ASIP is then placed in a low-power mode for a specified period, whereupon it repeats the profile cycle. Two-way communication over the Iridium network allows mission parameters to be changed in real time. ASIP has been used to study several scientific questions, such as the impact of diurnal warming on atmospheric processes, turbulence scaling in the upper ocean, parameterizing air–sea gas exchange, salinity gradients in the ocean surface boundary layer (OSBL), and consequences for remote sensing.

1. Introduction

The ocean and atmosphere form a coupled system. Properties are transferred between these two fluids through the action of the air–sea fluxes of momentum, mass, and heat. Understanding momentum exchange is important for modeling the circulation of the atmosphere and ocean (Stewart 1974) and for predicting their future states toward understanding climate (Donelan et al. 2004). Air–sea gas exchange contributes to the

reduction of greenhouse gases in the atmosphere by absorbing excess amounts of CO₂ (Wanninkhof et al. 2009). Increasing our understanding of air–sea transport requires measurement of the key parameters within the ocean surface boundary layer (OSBL). The upper few meters of the ocean form a critical interface for air–sea interaction, but due to observational challenges this region is greatly undersampled compared with the bulk of the ocean. The physical processes controlling momentum transfer, gas exchange, and radiative transfer are all concentrated on different spatial scales in the upper few meters ranging from millimeters to centimeters, leading to a high degree of heterogeneity that typically increases as one approaches the surface.

In the absence of suitably resolved measurements, available data from 10-m depth are frequently taken as representative for the entire surface layer (Ward et al. 2004), a practical approximation that may severely

[@] Current affiliation: Department of Mathematics, University of Oslo, and Norwegian Meteorological Institute, Oslo, Norway.

Corresponding author address: Brian Ward, School of Physics, National University of Ireland, Galway, University Road, Galway, Ireland.
E-mail: bward@nuigalway.ie

misrepresent the actual situation in this high-gradient region. Understanding interfacial processes also provides a linkage between satellite and in situ measurements. There now exists the capacity to measure sea surface salinity from space (Reul et al. 2012), in addition to the more established measurement of sea surface temperature. Global ocean models usually have a surface vertical resolution of only 10 m (Masson et al. 2012), prohibiting the explicit resolution of important processes for ocean–atmosphere coupling, such as diurnal cycling of the mixed layer (Janssen 2012); thermal (Minnett et al. 2011) and haline (Zhang and Zhang 2012) skin layer effects; and the vertical distribution of momentum by near-surface turbulence (Kudryavtsev and Soloviev 1990).

Understanding the processes controlling air–sea exchange in the very first centimeters of the ocean is also important from a climate perspective. Sea surface temperature (SST) influences the lower boundary layer for the atmosphere. Deep atmospheric convection is very sensitive to small temperature variations above the 28.5°C threshold (e.g., Gadgil et al. 1984; Graham and Barnett 1987). In tropical regions, the diurnal cycle of SST can strongly interact with convection and hence with large-scale phenomena like the Madden–Julian oscillation (e.g., Bellenger et al. 2010). Some other studies find that resolving the diurnal cycle of SST can induce a more consistent restitution of air–sea feedbacks and hence lead to an improvement of El Niño simulation (Masson et al. 2012).

Increasing the comprehensiveness of oceanographic observational datasets under a variety of environmental conditions will provide the information necessary to test existing hypotheses concerning the dynamics of the ocean boundary layer. This has the potential to lead to the development of new theories for understanding fluxes across the ocean surface; the interactions between currents, the SOBL, and the surface wave field, including wave breaking and the injection of turbulence; interactions between breaking waves and Langmuir cells; and interactions between SOBL dynamics, waves, and horizontal ocean fronts in regions where both turbulence and submesoscale dynamics are important. Such datasets would provide a stringent metric for verification and validation of emerging numerical models for the next decade. These efforts would lead to improved modeling of the upper-ocean mixed layer incorporating waves, and the lower atmospheric boundary layer.

Turbulence in the upper ocean, induced by wind shear, breaking waves, and buoyancy flux, periodically erodes the hierarchy of molecular sublayers immediately below the air–sea interface. The viscous, thermal, haline, and diffusive sublayers control the air–sea fluxes of momentum, heat, water, and gas (Lorke and Peeters 2006), but turbulence in the upper ocean, induced by

wind and Stokes shear, breaking waves, and convection, periodically erodes the hierarchy of molecular sublayers immediately below the air–sea interface. The greater the amount of turbulence, the more enhanced are the fluxes between the ocean and atmosphere. The nature of turbulence is such that energy is transferred from larger to smaller scales until they are dissipated by viscosity, and the kinetic energy is transferred into heat (Thorpe 2004). This is measured by estimating the rate of dissipation of turbulent kinetic energy (ϵ) per unit mass (units of energy per unit mass per unit time, or $\text{m}^2 \text{s}^{-3}$). Therefore, it is critical to quantify the turbulence at the ocean surface, which is a controlling process for air–sea exchange (Zappa et al. 2007), although there have been very few measurements in this region of the ocean. Agrawal et al. (1992) has shown enhanced dissipation at the surface that was attributed to breaking waves.

The development of vertical ocean profilers has largely been driven by the microstructure community, who are concerned with small-scale temperature, salinity, shear, and velocities in the ocean, which are vital for the study of ocean mixing and turbulence (Agrawal and Williams 1999). Although most of the microstructure profiling instruments have been developed in the descending mode, there have been only a few instruments that ascend through the water column. The profiler described by Caldwell and Dillon (1981) was most often deployed in the descending mode, but it also has the ability to profile upward. Using this mode, Dillon et al. (1981) described the results from an experiment where ϵ was found to scale according to atmospheric laws. Carter and Imberger (1986) describe the rising microstructure profiler (RMP), whose design criteria included ease of deployment so that the researcher in the field could analyze the data in real time and determine where the most interesting processes occurred for sampling. Sensors were limited to temperature and conductivity, and the main scientific focus was to study fine-structure and microstructure events associated with overturning. Soloviev et al. (1988) described an upward profiler that dropped a weight once it descended to the desired depth and came to the surface under its own buoyancy. Microstructure measurements were carried out with a 3D electromagnetic sensor, and these data provided verification to the near-surface bow sensors strapped to the ship. Anis and Moum (1995) describe the Chameleon profiler that was also deployed from a ship, lowered to a depth of 120 m, whereupon a weight was released, allowing the profiler to ascend to the surface. Stevens and Smith (2004) deployed a Self-Contained Autonomous Microprofiler (SCAMP) in an upward mode using a pulley system [similar to the one described by Mammen and von Bosse (1990)] to make temperature microstructure measurements in the upper few meters. Ward et al. (2004) described the Skin Depth Experimental

TABLE 1. Specifications for the core sensors on ASIP. Asterisk denotes two sensors.

Parameter measured	Manufacturer and model	Resolution	Precision/accuracy/noise	Purpose
Pressure	Keller 30X	0.002%	Accuracy: 0.1%	Depth and rise velocity
Temperature	Rockland FP07-38*	0.0001°C	Precision: 0.1°C	Microstructure temperature variance, density determination
Temperature	NBOSI CT	0.0001°C	Precision: 0.001°C	Temperature calibration reference
Temperature	Aanderaa 3830	0.01°C	Accuracy: 0.05°C	Secondary calibration reference
Conductivity	Rockland SBE 7	−3 dB at 100 cpm	Noise: $2 \times 10^{-7} (\text{S m}^{-1}) (\text{Hz})^{-1/2}$	Surface detection, salinity and density determination
Conductivity	NBOSI CT	0.000 01 S m^{-1}	Accuracy: 0.0003 S m^{-1}	Conductivity calibration reference
Shear	Rockland SPM-38*	10^{-4} s^{-1}	Accuracy: 5%	Estimates of dissipation
Oxygen	Aanderaa 3830	<1 μM	Accuracy: <8 μM	Determination of oxygen concentration
PAR	LI-COR LI-192	250 $\mu\text{mol s}^{-1} \text{ m}^{-2}$	Accuracy: 2%	Light absorption
Acceleration x, y, z	Measurement Specialties M4000	0.01 g	Accuracy: 0.1 g	Orientation of ASIP
Acceleration x, y, z	MicroStrain 3DM-GX2	0.01 g	0.2%	Orientation of ASIP
Angular rate x, y, z	MicroStrain 3DM-GX2	0.2 s^{-1}	0.2%	Orientation of ASIP

Profiler (SkinDeEP), which was autonomous and could ascend from about 10 m below to the surface with an inflatable sleeve to change its buoyancy. There is also the Argo float program, which consists of a global array of vertically ascending profilers with mean temperature and salinity sensors (Roemmich and Owens 2000). The Argo instruments do not sample all the way to the surface, as there is the risk of contaminating the pumped conductivity cell, and so this is switched off at 10 m.

Although several of the ascending profilers are capable of making microstructure measurements at the ocean surface, none of them was autonomous and several contained only scalar sensors. There was also the concern of flow distortion when deploying a microstructure profiler attached to a vessel; the ship-induced contamination may be indistinguishable from wind mixing (Hodges and Fratantoni 2014). These concerns led to the development of the Air–Sea Interaction Profiler (ASIP), the first autonomous instrument capable of making ascending profiles of microstructure shear, temperature, and conductivity, as well as several other important physical properties. The primary focus of the instrument is within the upper 10 m of the ocean, but it can profile to a maximum depth of 100 m and so it can include mixed layer studies. As such, ASIP is a versatile instrument that can be directed toward the study of processes within the water column, as well as the air–sea interface. To avoid contamination from shipboard deployments, ASIP was designed to be autonomous, and once deployed it can conduct a preprogrammed mission to capture repeated profiles of data in the upper ocean.

In this paper, a detailed description of the Air–Sea Interaction Profiler is presented, including design considerations, operation, and performance. An overview of ASIP and the data processing, which addresses issues of converting the data to quantitative measurements of key properties of the upper ocean, is provided in section 2. Section 3 presents examples of the data acquired during several of its field measurement campaigns. A summary of the paper is provided in section 4. The appendixes to the paper provide the descriptions of the mechanical, electrical, and software of ASIP, and details of data recording and the onboard software for mission control and data storage.

2. ASIP

a. ASIP overview

Motivated by fundamental questions of air–sea exchange, ASIP was designed to study the surface layer of the ocean with an integrated suite of small-scale measurements from a single upwardly rising and autonomous platform. Every effort was made to populate ASIP with the highest-resolution sensors available. ASIP has sensors for pressure, microstructure shear, microstructure, and accurate response temperature and conductivity; three-dimensional (3D) orientation and acceleration; photosynthetically active radiation (PAR); and dissolved oxygen (Table 1). Autonomous operation was a critical element of the design specification, as this permits repeated and undisturbed measurements in the uppermost levels of the ocean, where the relevance of the small scales becomes ever more important as the air–sea interface is approached.

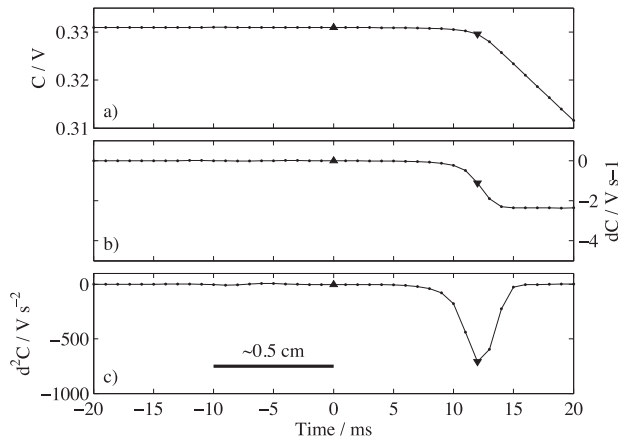


FIG. 1. Surface detection procedure: (a) uncalibrated conductivity signal (V) as a function of relative time from the determined surface (ms), (b) time derivative of the conductivity, and (c) second time derivative of the conductivity. The up (\blacktriangle) and down (\blacktriangledown) solid triangles indicate the minimum second derivative of the raw conductivity signal and the surface, respectively.

The instrument is positively buoyant, and for each profile ASIP dives using three thrusters (SeaBotix BTD150) to a maximum depth of 100 m. Once the desired depth has been reached, the thrusters cease operation, and the instrument then ascends through the water column under its own buoyancy. Data are acquired throughout the ascent until the sensor package breaks through the free surface. ASIP transmits a short message upon completion of the profile using the Iridium short-burst data (SBD) messaging service (alternatively, this may occur after a prescribed number of *rapid* profiles, which will be described in more detail in [appendix B](#)). Two-way communication allows the mission settings to be reprogrammed in real time. The battery lifetime allows for a total of roughly 6000 m of cumulative profiling per deployment, for example, approximately 60 profiles from the maximum depth of 100 m. At the end of its mission ASIP remains on the surface, periodically transmitting its position. Deployment and recovery are both accomplished manually from a small boat.

b. ASIP surface detection

An important aspect of conducting air–sea interfacial measurements is the ability to accurately determine the location of the free surface. This is carried out with the microconductivity sensor because it has a spatial response $O(10^{-2}\text{ m})$ and exhibits an abrupt drop-off when it crosses the air–sea interface.

Figure 1a shows the uncalibrated conductivity signal (in volts) with respect to time. The position of the surface is calculated in two steps (Fig. 1): first, the minimum of the second derivative is located; this exists just after ASIP exits the water. Second, the last point where the

conductivity signal is constant is determined, based on a threshold estimated from the local variance—that is, the threshold is calculated as one-sixth of the standard deviation of C from 2 to 0.5 s before the local minima in the second derivative. The time and the one-sixth factor have been determined empirically from studying hundreds of profiles and have been shown to give robust results within 1 cm of what appears to be the surface. If required, further refinement is conducted after manual inspection of each parameter in the profile.

c. ASIP dissipation estimates

The microstructure shear, which can be related to turbulence levels, is measured with the airfoil shear probe, which has been described in detail in the literature (e.g., [Oakey and Elliott 1982](#); [Osborn and Crawford 1980](#); [Lueck et al. 2002](#); [Macoun and Lueck 2004](#)). ASIP is equipped with two shear probes (SPM-38), which are provided by Rockland Oceanographic Services Inc. The analog signals from these sensors are amplified and conditioned with low-noise analog circuit boards also provided by Rockland, and subsequently digitized and fed into the data stream (see [appendix D](#)). The two shear probes are oriented at 90° to each other, so as to provide for orthogonal components of the microstructure shear and to evaluate the assumption of isotropy. The sensor consists of a bullet-shaped rubber tip that houses a piezoceramic beam. A voltage E_p is produced as the beam bends from turbulence-induced eddies: $E_p = \hat{s}Wu$, where \hat{s} is the probe sensitivity (provided by the manufacturer after calibration), W is the velocity of the sensor transported by ASIP through the water column, and u is the cross-axial velocity fluctuation produced by the water current transverse to the direction of the shear probe. The shear signal $\partial u / \partial z$ is given by

$$\frac{\partial u}{\partial z} = \frac{1}{W} \frac{\partial u}{\partial t} = \frac{1}{\hat{s}W^2} \frac{dE_p}{dt}. \quad (1)$$

For isotropic turbulence regimes, the turbulent dissipation rate ε can be calculated ([Yamazaki and Osborn 1990](#)) with Eq. (1):

$$\varepsilon = 7.5\nu \overline{\left(\frac{\partial u}{\partial z}\right)^2}. \quad (2)$$

To calculate ε from Eq. (1), there are several steps taken in postprocessing to ensure a good signal, namely, the following:

- (i) To remove spikes from the signal, usually due to the probe encountering plankton or other detritus in the water column, the algorithm compares the

raw shear with the shear low-pass filtered at 1 Hz. If the raw signal is 10 times greater than the low-pass signal, then it is removed and replaced with the mean of the surrounding 10 points.

- (ii) The shear signal is high-pass filtered at 0.5 Hz to remove the mean from the signal.
- (iii) The power spectral density estimate is calculated with a 512-point fast Fourier transform on 1024-point segments with a 256-point Hanning window applied to each.
- (iv) Spectra are corrected for spatial averaging arising from the fact that the shear probe tip is typically larger than the smallest eddies encountered using the form of a single-pole low-pass filter (Oakey and Elliott 1982; Macoun and Lueck 2004).

Once the power spectral density estimates are obtained, ε is then determined by integrating the spectra over the resolvable wavenumbers, using either the Nasmyth or Panchev–Kesich spectrum to extrapolate to higher and lower wavenumbers (Moum et al. 1995; Gregg 1999).

A recursive algorithm similar to Moum et al. (1995) to integrate the power spectra is used to ensure that the computed ε converges to the actual value. First, the spectra are integrated between 2 and 15 cycles per meter (cpm) and ε is estimated from Eq. (2). This is used to calculate an initial estimate of the Kolmogorov wavenumber k_ν , which is the wavenumber where viscosity effects begin to dominate energy dissipation and is written as

$$k_\nu = \frac{1}{2\pi} \left(\frac{\varepsilon}{\nu^3} \right)^{1/4}, \quad (3)$$

where ν is the kinematic viscosity. If $k_\nu > 15$ cpm, then the upper wavenumber is increased and ε is calculated again. This process is repeated until the cutoff wavenumber is within 2 cpm of the last computed value of k_ν .

Three spectra corresponding to three different depths are shown in Figs. 2b, 2c, and 2d. The integration limits for each spectrum are shown by the triangles, and k_ν is denoted by the vertical dashed line.

From inspection of the shear profile (Fig. 2), it can be seen that within the wave boundary layer (between the air–sea interface and approximately 10-m depth), the shear exhibits a low vertical spatial signal in addition to the characteristic high-frequency signal of active mixing generated by turbulence. The mixing layer extends to about 28 m, but below this there is very little turbulence. Measurements in this region are on the order of $10^{-10} \text{ m}^2 \text{ s}^{-3}$ (Fig. 2c), which represents the noise level for dissipation estimates. The region of high shear at the base of the profile is the remnants of the wake of ASIP's thrusters.

As ASIP rises it exits this thruster turbulence within 10 m of the base of the profile.

The pressure sensor on ASIP not only provides the depth information but also the determination of the rise velocity, which is an important parameter for calculating dissipation from the shear signal. According to Eq. (1), the small-scale shear measurements ($\partial u / \partial z$) are proportional to $1/W^2$, and from Eqs. (1) and (2), it is seen that ε is proportional to $1/W^4$. Therefore, careful estimation of W is required, which is determined from the time derivative of the ASIP pressure signal initially low-pass filtered at 5 Hz (Fig. 3a). ASIP does not reach its terminal velocity of 0.5 m s^{-1} for several meters after the beginning of its ascent, after which it remains relatively constant until ASIP enters the wave boundary layer at about 10 m. This is highlighted in Fig. 3b, which shows the percentage variation of W from the mean. The percentage root-mean-square (rms) of the variation in W in the upper 40 m, calculated and averaged over all profiles, was 2.5%. In the upper 5 m the average rms was 8%, between 5 and 10 m the rms decreased to 3.4%, and between 10 and 40 m the rms decreased further to 1.4%. Figure 3c shows the pitch and roll for the same ASIP profile as in Fig. 3a. The largest pitch and roll values occurred in the upper 5 m and were on the order of $\pm 5^\circ$ over distances of 2–2.5 m. The rms value of pitch and roll within the upper 40 m averaged over all profiles was below 0.7° for each. Specifically, in the upper 5 m this value was below 1.7° . Between 5 and 10 m, this decreased to below 0.83° and further decreased to below 0.5° at depths between 10 and 40 m.

To investigate the effect of a varying W when estimating ε , we employed three different estimates of W : block (blk), global (glob), and instantaneous (inst). In the block approach, the W and shear profiles were divided into nonoverlapping blocks of 512 points and the average rise velocity of each block was used to convert the corresponding block of shear data into physical units. In the global approach, a single representative value of W for each profile was used, which was calculated as the average W value from 20 to 30 m. This depth region was chosen because it had consistently stable rise velocity and excluded the extremes of the profile. For the instantaneous approach, the instantaneous value of W was used on a point-by-point basis. For the block and instantaneous approaches, shear power spectra were converted from frequency space to wavenumber space using an average value of W calculated over all data points within each segment of data and so varied over the entire profile. In the global approach, W remained constant for this conversion process. Figure 4 shows the histograms of the percentage difference for $\varepsilon_{\text{blk}} - \varepsilon_{\text{glob}}$ and $\varepsilon_{\text{block}} - \varepsilon_{\text{inst}}$: for the former, 94% differ by less than $\pm 20\%$ and 99.5% differ by less than $\pm 50\%$. For the

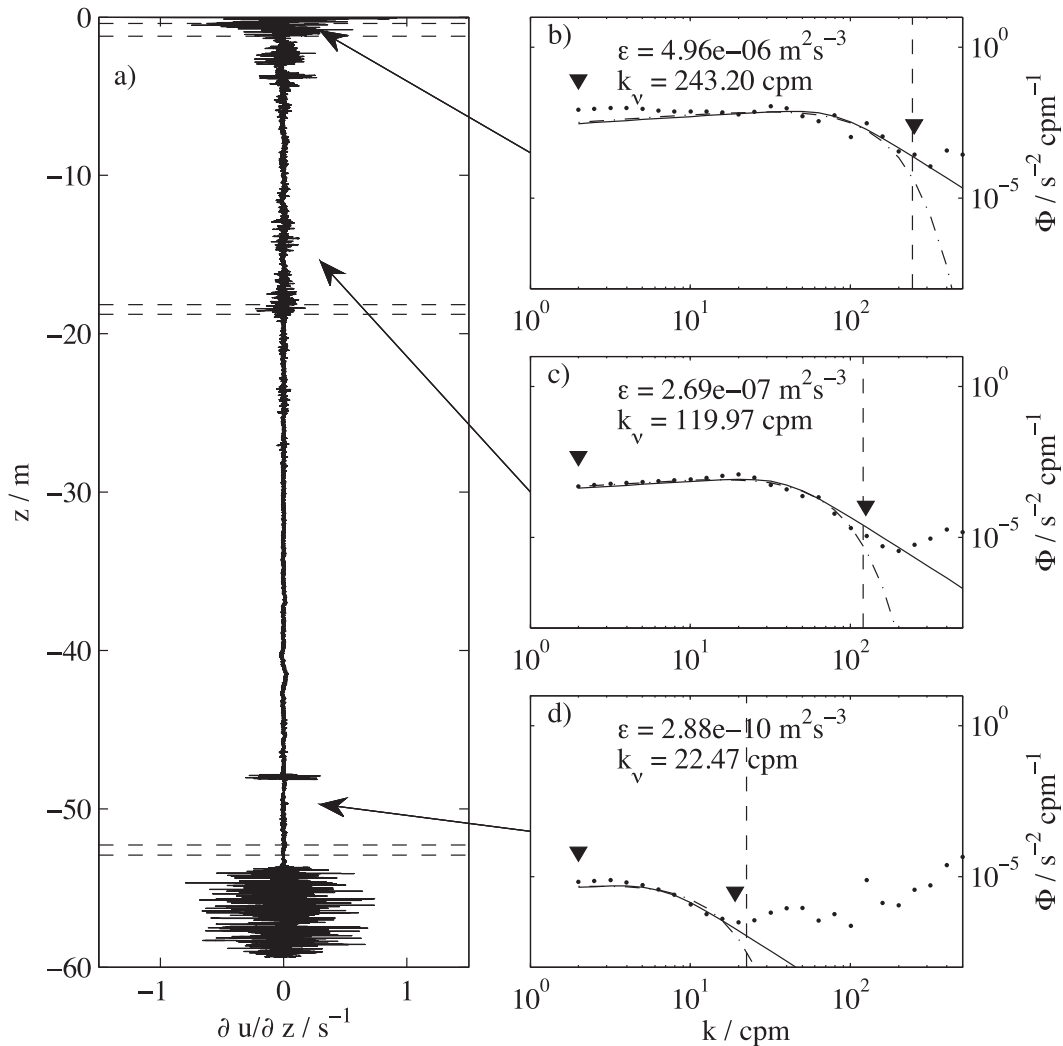


FIG. 2. (a) ASIP shear profile from the subtropical Atlantic. (b), (d) Shear power spectra (solid points) for the sections indicated (b = surface, c = 18 m, d = 53 m). The solid and dashed-dotted lines denote the Nasmyth and Panchev-Kesich spectra, respectively. The down solid triangle (\blacktriangledown) indicates the integration limits, and the vertical dashed line is the Kolmogorov wavenumber.

latter 99.9% differ by less than $\pm 20\%$. The variation in the values of ε was on the order of 50% for the vast majority of data points, which is much less than the order of magnitude variation of ε due to natural variability and patchiness. Based on this analysis, we use values of ε calculated via the block approach.

Figure 5 shows the distribution of the squared shear signal from 82 profiles in the subtropical Atlantic for the two shear probes (Figs. 5a and 5b). There are some distinct features: at the base of the profile there is enhanced turbulence, which arises from ASIP moving through its own thruster wake; at the surface there is also enhanced turbulence, where the upper ocean directly experiences the energy input from the atmosphere.

d. Calibration

ASIP is equipped with two FP07 microstructure temperature (T_μ) sensors and a Sea-Bird Electronics SBE 7 microstructure conductivity (C_μ) sensor (both provided by Rockland and repackaged to fit the SPM-38 shear probe holder). One of the FP07s is oriented in the upright mode, and the other is mounted at an angle so as to position itself close to the SBE 7 conductivity sensor, thereby minimizing the spatial incoherence. Synchronization of the C_μ and T_μ sensors is conducted by cross correlating the time derivative of these two signals to produce a quality salinity measurement. Poorly synchronized temperature and conductivity signals can produce unrealistic spikes in the salinity

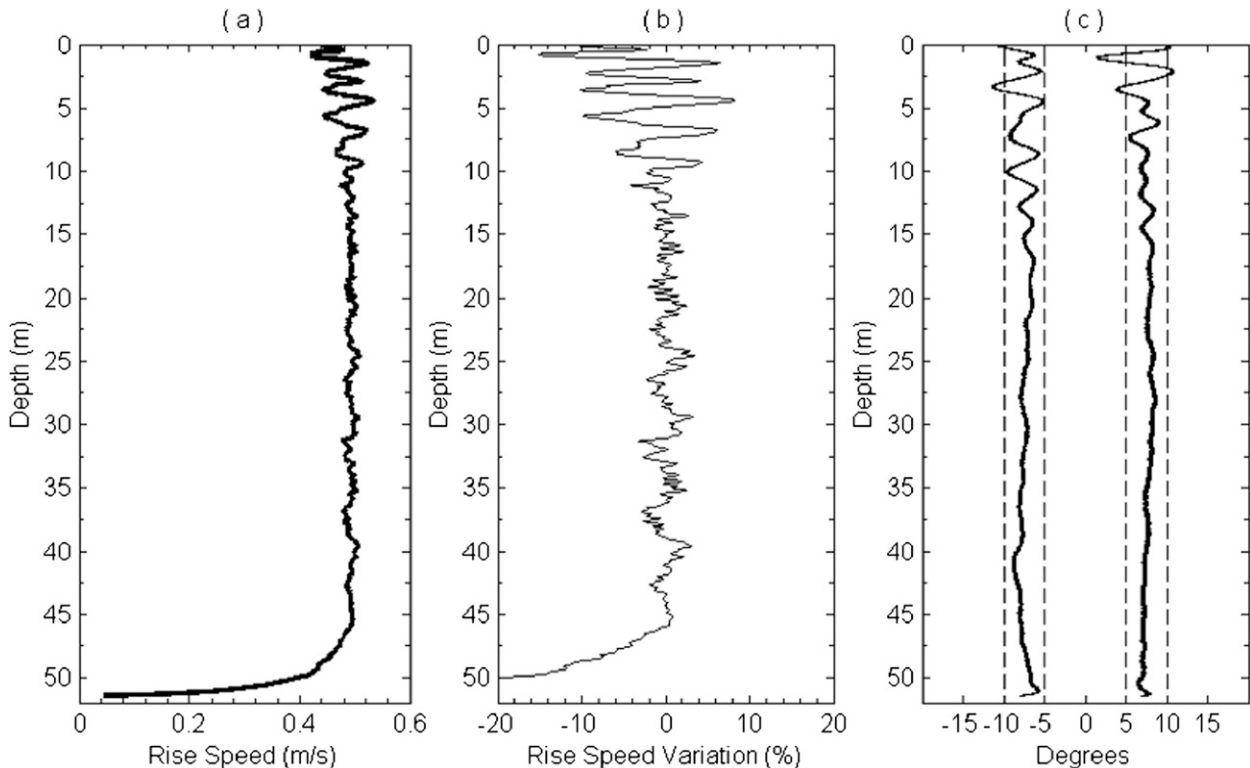


FIG. 3. (a) ASIP rise speed (W) for a single profile. (b) Percentage variation of W . (c) ASIP pitch offset by -7.5° (left line) and ASIP roll offset by $+7.5^\circ$ (right line).

signal (Garau et al. 2011). This postprocessing step is carried out for every single ASIP profile.

Figure 6a shows a typical example of the cross-correlation $C_{xx}(T, C)$ as a function of the lag. The maximum cross-correlation value gives the shift between the signals, which has then been fitted with a Gaussian curve. In the example shown in Fig. 6a, the conductivity is shifted ahead by 13 sampling points, which in fact turned out to be

representative of all the profiles. From analysis of several profiles, the mean shift was found to be 12 ± 1 . After calculating the shift, the temperature can be synchronized with the conductivity. Figure 6b shows an example of a section of a profile for the synchronized temperature and conductivity in arbitrary units (i.e., before calibration).

Calibration drift is inevitable with T_μ and C_μ sensors, and so ASIP is also equipped with a Neil Brown Ocean

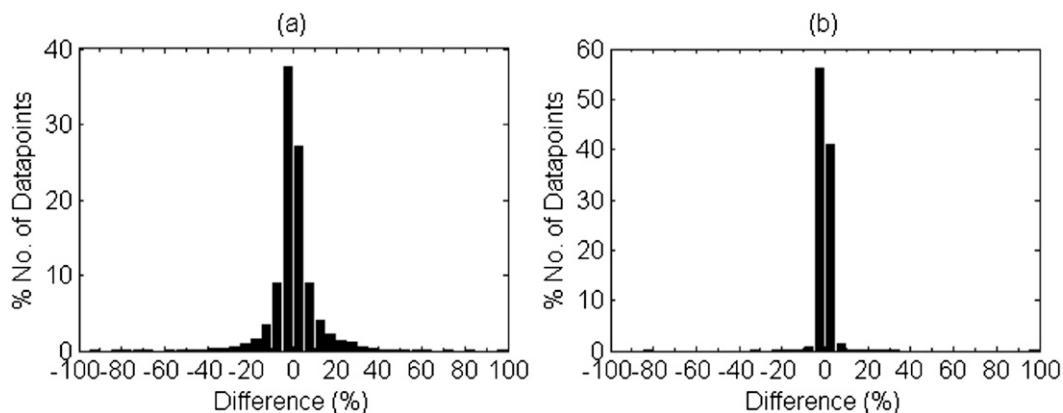


FIG. 4. (a) Percentage difference between ϵ calculated using the block approach and the global approach. (b) Percentage difference between ϵ calculated using the block approach and the instantaneous approach. The bin sizes are 5%.

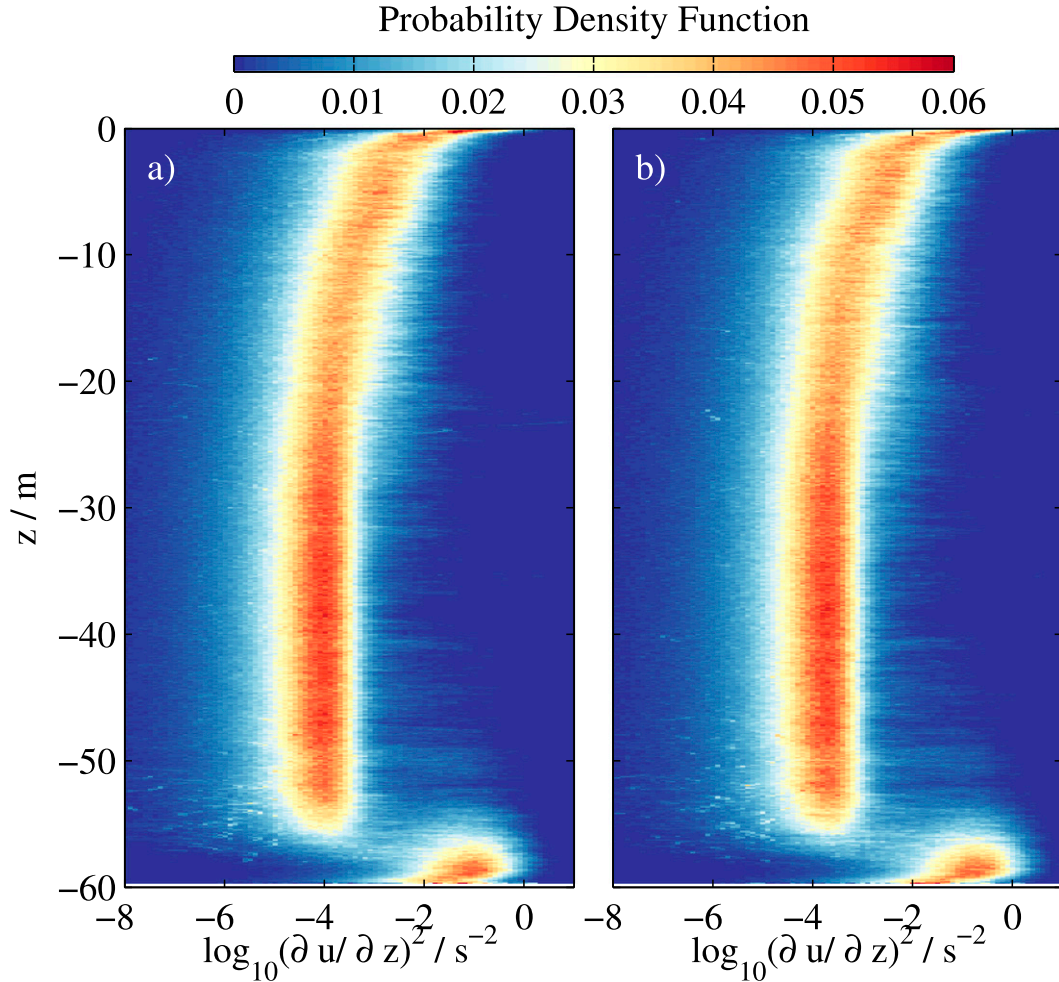


FIG. 5. (a),(b) Distribution of shear data for each shear probe as a function of depth from a single deployment of 82 profiles in the subtropical Atlantic. The enhanced turbulence from the thruster is clearly seen at the base of the profile. It is also apparent that there is an enhanced shear signal as the surface is approached. The probability density function (pdf) is normalized by the number of measurements at each depth interval.

Sensors, Inc. (NBOSI) glider CTD (G-CTD) sensor (see Fig. 13) to provide in situ calibrations, which can be applied to the data after acquisition. This sensor was developed for autonomous underwater vehicles (AUVs) and gliders with specifications of low drag, low power, high resolution, and no pumping. Figure 7 shows the process of calibrating the T_μ and the C_μ sensors against the NBOSI temperature T_{ref} and conductivity C_{ref} . Both microsenors are sampled as analog signals at 1000 Hz, whereas the NBOSI sensors have digital outputs with an update rate of 10 Hz, and so T_μ and C_μ are decimated to 10 Hz. The reference and microsenors are then aligned according to the maximum of the cross correlation, shown in Fig. 7a for temperature and Fig. 7d for conductivity. In all the cases (i.e., all deployments and profiles), the difference between the thermal and conductivity shift is three sampling points, indicating

that there is a small spatial misalignment between T_{ref} and C_{ref} (T_μ and C_μ have been previously aligned as described above).

Figures 7b and 7e show the process of calibration with a first-order polynomial, which is used to obtain physical units from the voltage outputs from the microsenors. Figures 7c and 7f show profiles of the NBOSI and microsenors in a region with a small gradient (SM). There are two statistical values that give us an indication about the goodness of the calibration: the mean absolute deviation (mad) between NBOSI and microdata, and the percentage (per) of the NBOSI data where there are small gradients. In the example shown in Fig. 7, the mad is $4\text{ m}^\circ\text{C}$ and $8\text{ }\mu\text{S cm}^{-1}$, and the per value is almost 100% for both cases. In general, the temperature calibration has a mad value of $\text{mad}_T < 0.005^\circ\text{C}$ and a per value of $\text{per}_T > 75\%$. Although the calibration

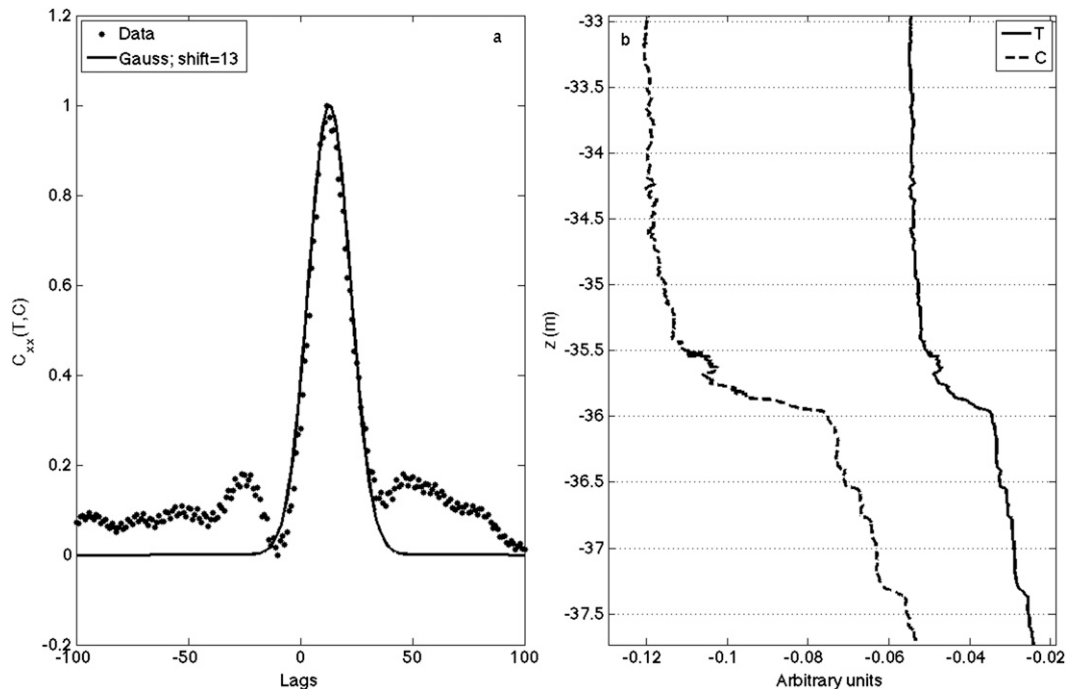


FIG. 6. (a) Cross correlation between the microtemperature and microconductivity. (b) Example of synchronized temperature and conductivity profiles. A horizontal grid has been added to allow comparison between the thermal and conductivity structures.

coefficients vary from one deployment to the next, they have proved to remain constant during each particular deployment. The conductivity, on the other hand, gives a smaller fraction with acceptable goodness parameters—that is, $\text{mad}_C < 0.01$ and $\text{per}_C > 75\%$, but per_C can be as low as 40%. Microconductivity calibrations change on a per profile basis, indicating that there is much more drift than the microtemperature.

3. Observations

To date, ASIP has been deployed during seven field experiments. Table 2 summarizes the field experiments in which ASIP has been involved along with the scientific objectives and environmental conditions. ASIP has been used to study several scientific problems, from diurnal warming (Vialard et al. 2009) to upper-ocean salinity to wave-induced turbulence (Sutherland et al. 2013, 2014; Callaghan et al. 2014).

The scalar microstructure sensors on ASIP can provide detailed measurements of processes at the ocean surface that would otherwise be masked with instruments such as a shipboard CTD and descending microstructure profilers. A good example of this is shown in Figs. 8a and 8b, which is a series of 10 profiles acquired off the New England shelf (Fig. 8c) in June 2011. ASIP was deployed to a depth of 20 m and the profile interval

was 5 min, providing a very detailed snapshot of the SOBL. The most striking feature of this time series is the presence of the freshwater layer in the upper 1.5 m. The presence of low-salinity water sitting at the ocean surface is often an indication of rain, but from the ship's [Research Vessel (R/V) *Knorr*] meteorological data, there was no record of rainfall at least within a day of this deployment. Reverdin et al. (2012) has shown that salinity anomalies between 0.15 and 0.5 m (measured with drifters) from rain events disappear after a typical period of 4 h. Also, freshening in the upper few meters of the ocean have been reported (e.g., Soloviev and Schlüssel 1996; Soloviev and Lukas 1997), but the magnitude of these events have been limited to a few tenths parts per trillion (ppt). It is not clear if this signal is a transient feature, or if there are any consequences for the large-scale transport, but it is unlikely that this freshwater signal would be captured without an instrument that has the measurement capabilities of ASIP.

ASIP is also ideally suited to study the response of the ocean mixed layer to changing atmospheric conditions. Sutherland et al. (2013) presented observations from ASIP in the mixed layer during the passage of a low pressure system over the region during the deployment. Figure 9 shows the results of 54 profiles (approximately 1 every 20 min) during the Bloomcruise at roughly 54°N, 46°W. The wind speed, referenced to 10-m height, is

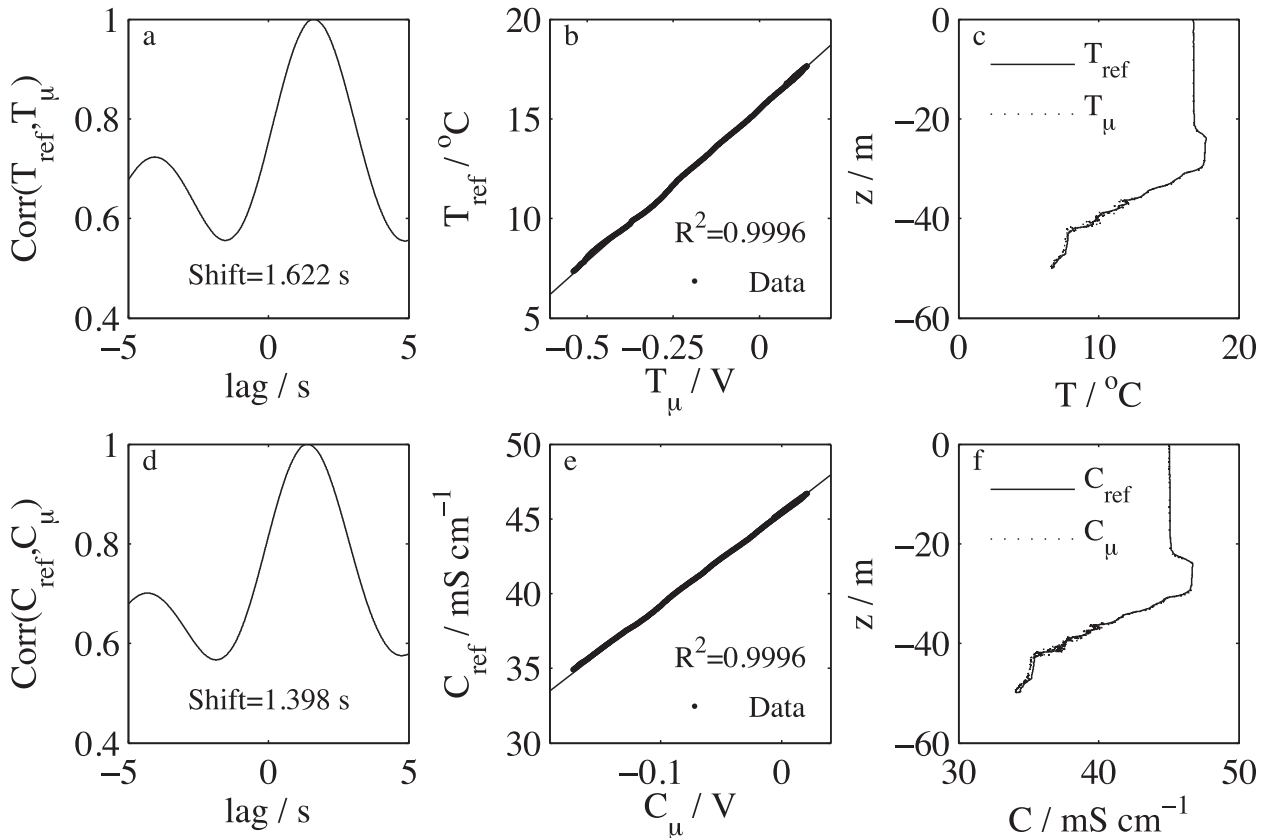


FIG. 7. Calibration of the T_μ and C_μ sensors with the NBOSI T_{ref} and C_{ref} data from a single profile. Cross correlation for (a) temperature and (d) conductivity. Data used for the polynomial, which are a subset of all the data points, for (b) temperature and (e) conductivity; the subset was chosen in regions where there were small gradients. Calibrated signal for (c) temperature and (f) conductivity.

shown in Fig. 9a. The wind speed is approximately 10 m s^{-1} from the beginning of the deployment to 2100 local mean time (LMT) at which the point the wind rapidly drops to $<5 \text{ m s}^{-1}$. ASIP is able to detect that ε (Fig. 9b) responds very quickly to this drop even if the mixed layer does not (black line in Figs. 9b and 9c). This is more clearly shown in Fig. 9c, where ε is normalized by the law of the wall, which is the well-established dissipation profile normal to a solid boundary given by

$$\varepsilon_\tau = \frac{u_*^3}{\kappa z}, \quad (4)$$

where u_* is the friction velocity, z is the depth, and κ is the von Kármán constant with a value of 0.4. ASIP is able to resolve these variations accurately and provides crucial measurements in the upper few meters that conventional profilers would not.

Stratification associated with diurnal warming is a process that occurs at the ocean surface and is important for the air–sea exchange of heat (Fairall et al. 1996; Ward 2006) and CO_2 (McNeil and Merlivat 1996). Diurnal warming occurs under conditions of low wind and intense downwelling irradiance, of which 40%–60% is in the infrared; this is almost completely (i.e., 99.9%)

TABLE 2. Summary of the ASIP deployments to date.

Date	Experiment	Location	Scientific objectives
Feb 2007	Cirene (R/V <i>Suroît</i>)	Indian Ocean	Impact of diurnal warming on atmospheric convection
May 2009	Gogasmos (R/V <i>Antea</i>)	Bay of Biscay	Upper-ocean salinity stratification
May 2010	Repeat transect (CCGS <i>Hudson</i>)	Labrador Sea	Surface freshening
Apr 2011	Oilwave (R/V <i>Johan Hjort</i>)	Lofoten (Westfjorden)	Surface wave-generated turbulence
Jul 2011	Bloomerise (R/V <i>Knorr</i>)	North Atlantic	Air–sea gas exchange
Aug 2012	STRASSE (R/V <i>Thalassa</i>)	Subtropical North Atlantic	Upper-ocean salinity
Apr 2013	MIDAS (R/V <i>Sarmiento de Gamboa</i>)	Subtropical North Atlantic	Upper-ocean salinity

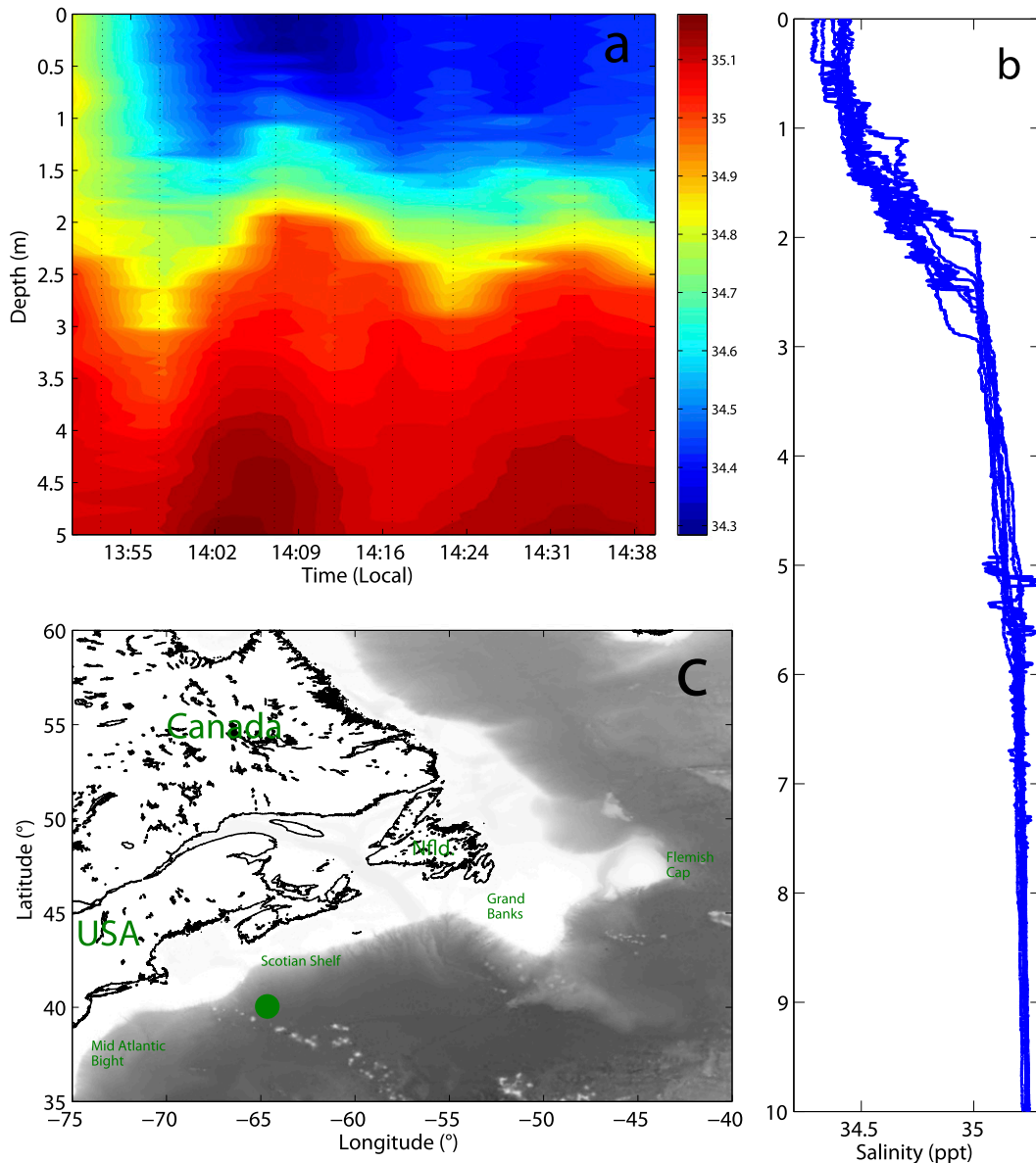


FIG. 8. (a) Ten salinity profiles in the upper 5 m of the ocean showing a very strong freshwater signal at the surface. (b) Individual profiles of salinity showing the freshwater lenses in the upper 3 m. (c) Location of the deployment (indicated by the dot) acquired in June 2011 in the North Atlantic.

absorbed within the upper 2 m (Sweeney et al. 2005). Conversely, higher wind speed increases the turbulence at the surface and enhances air–sea heat exchange, preventing the establishment of thermal stratification. Webster et al. (1996) defined several bulk temperatures that exist—true, buoy, and ship, corresponding to depths of 0.1, 0.5, and 5 m, respectively. Donlon et al. (2002) further refined these temperatures as SST_{subskin} , $SST_{0.5\text{m}}$, and $SST_{5\text{m}}$, which emphasized the need to define the depth of measurement. Large diurnal warming amplitudes (2° – 3°C) have been determined with thermometers

at a fixed depth, infrared radiometers, research vessels' thermosalinographs, and moorings (e.g., Price et al. 1987; Webster et al. 1996; Minnett and Ward 2000; Gentemann and Minnett 2008; Kawai and Kawamura 2002). However, these measurements cannot provide a picture of the stratification below the surface. For example, Soloviev and Lukas (1997) showed extreme warming from an upwardly rising profiler under no-wind conditions. Ward (2006) defined the warm layer $\Delta T_w = T_{\text{subskin}} - T_{z_r}$, where T_{z_r} is the temperature at a reference depth, and showed very strong warming

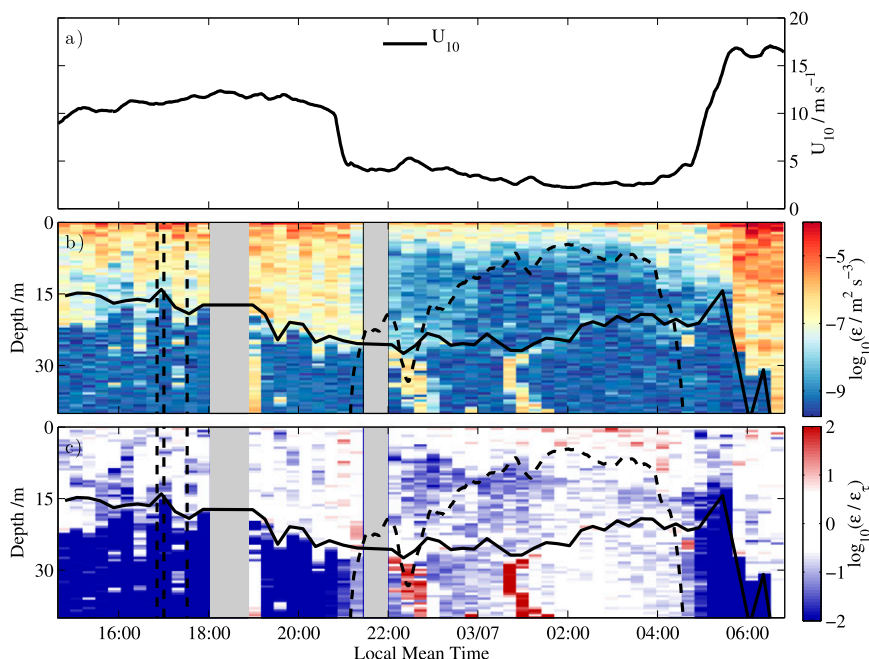


FIG. 9. (a) Wind speed U_{10} . (b) Turbulent dissipation rate ϵ . (c) Dissipation rate normalized by the law of the wall [given by Eq. (4)]. The solid black line in (b),(c) denotes the mixed layer depth, and the dashed line in (b),(c) is the Monin–Obukhov length. All times have been converted to LMT.

in the upper 1 m, which had a significant effect on the net air–sea heat flux.

ASIP lends itself to the study of diurnal warming, and Fig. 10 shows four individual profiles acquired over 1 h in the subtropical North Atlantic, where conditions were conducive to strong warming within the upper 2 m. The magnitude of ΔT_w was $>1^\circ\text{C}$, and the temperature profile from the FP07 thermistor indicates that there were periods of temperature microstructure (e.g., 1242 at 2 m and 1335 at 2–4 m). The occurrences of high temperature variability coincide with high levels of dissipation, derived from the shear probes.

4. Summary

This paper describes the Air–Sea Interaction Profiler, which was developed to study the near-surface ocean layer with a suite of high-resolution sensors. One of the unique characteristics of ASIP is the fact that it can take measurements at the air–sea interface with sub-centimeter resolution. It has the advantage that it is completely autonomous and Lagrangian, providing undisturbed measurements in the open ocean.

There is little doubt that small-scale measurements in the upper few meters of the ocean are important, as quantification of the processes near the air–sea interface is critical for describing atmosphere–ocean exchange.

This was the motivation for the development of ASIP, which in this respect is a unique and versatile instrument for studies operating over mixed layer depths to the ocean surface.

ASIP has a core suite of microstructure sensors to provide estimates of the rate of dissipation of turbulent kinetic energy and small-scale temperature and salinity (in combination with the CTD-quality data for in situ calibration). These are fundamental processes for air–sea exchange, and much of the effort in developing the data processing has been dedicated to utilizing the best techniques for processing the data.

The extended suite of sensors mounted on ASIP provides a rich dataset with which to study a variety of scientific questions from a single platform. To date, data from ASIP has been used to investigate ocean surface processes, such as diurnal warming at the ocean surface, internal breaking waves, surface scaling of dissipation at the ocean surface, the time response of the upper ocean to atmospheric forcing, and salinity gradients.

ASIP's deployment mission is fully controlled with an onboard embedded computer that can run a set of user-specified parameters specifying the number of profiles, the depth of each profile, and the profile interval. These parameters can all be changed during deployment in real time using the Iridium short-burst data protocol. This feature adds significant flexibility to a mission; for

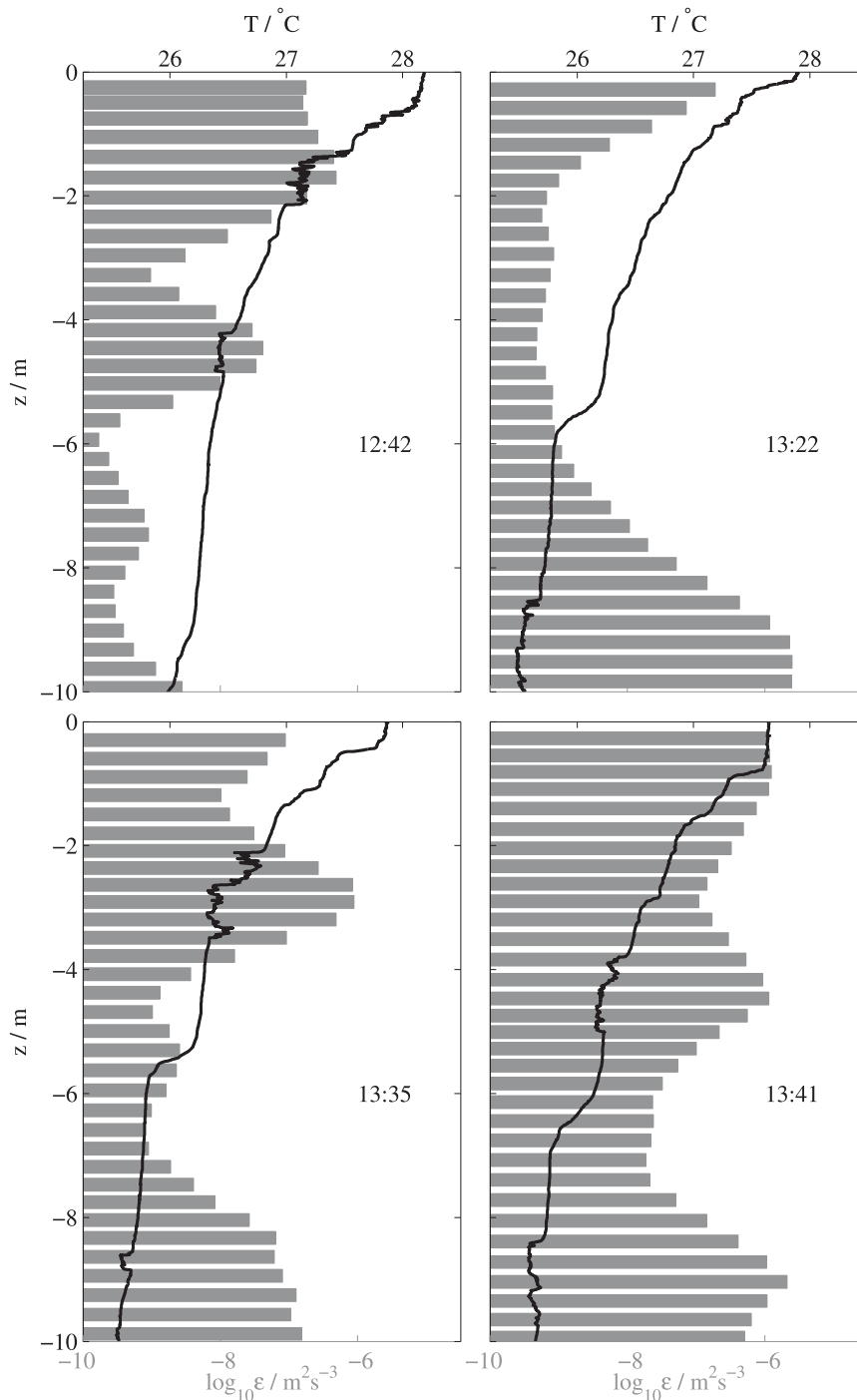


FIG. 10. Stratification captured by ASIP over a single hour during the Subtropical North Atlantic Salinity Experiment (STRASSE) in August 2012. Temperature microstructure corresponds to local peaks in the dissipation profile.

example, if the mixed layer were to shoal (as is often the case during daytime stratification), then the profile depth of ASIP could be changed to remain closer to the surface, thereby saving energy and extending the deployment (submerging ASIP with the thrusters is the

largest drain on the batteries, and therefore shallow profiles allow either higher-frequency sampling or longer deployments).

Following in the same spirit as [Caldwell and Dillon \(1981, p. 1\)](#), “Continuing evolution is expected, and no

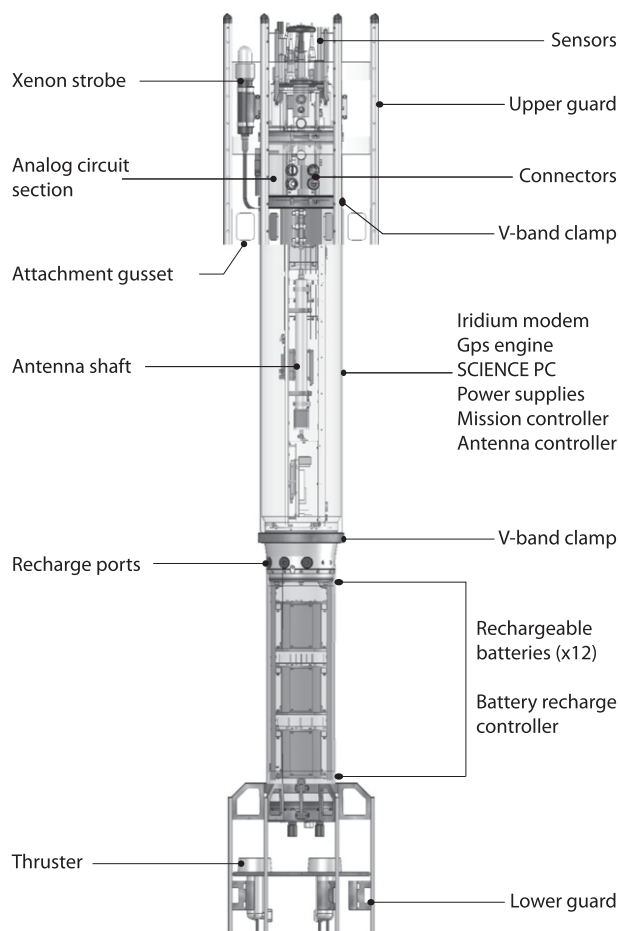


FIG. A1. Schematic of ASIP showing the major components of the instrument.

final form of the beast is anticipated,” ASIP continues to be an experimental instrument. We anticipate expanding the sensor suite in the future to include biological measurements such as fluorescence, which would allow us to quantify chlorophyll. The combination of turbulence and chlorophyll data would allow studies into thin layers, where plankton congregate in layers that are $O(1\text{ m})$ in the vertical but can extend for kilometers in the horizontal. Here organisms are orders of magnitude greater in abundance than outside the thin layer (McManus et al. 2003). Several studies have shown that turbulence can impact biological size and growth rate, as well as affect the delivery of nutrients and light (Wang and Goodman 2009). Measurements of color-dissolved organic matter in the upper ocean would allow us to distinguish between freshwater lens that originate from rivers and rainwater (see Fig. 8). This would be valuable for studying the air–sea freshwater budget in the open ocean (Hu et al. 2004), and would help improve estimates of salinity from space with the National Aeronautics and Space Administration’s (NASA)

Aquarius satellite and the European Space Agency’s (ESA) Soil Moisture and Ocean Salinity (SMOS) satellite. As new sensor technology becomes available, the design of ASIP lends itself to the ease of integration of these new sensors, which will undoubtedly provide new insights into upper-ocean processes.

Acknowledgments. The development of ASIP was supported by NSF Grant OCE–0241834. The Cirene cruise was supported by NSF Grant OCE–0629707. The Labrador Sea cruise was supported by NSF Grant OCE–1036097 and NUIG Millennium fund RM0908. The Strasse campaign was supported by the Office of Naval Research through Grant N62909-12-1-7064 and by the European Space Agency under ESRIN/Contract 4000102925/11/I-AM. B. Ward acknowledges the fellowship support of the Marie Curie International Reintegration Grant IRG-224776. G. Sutherland thanks the National Sciences and Engineering Research Council of Canada for funding support. A. H. Callaghan acknowledges financial support from the Irish Research

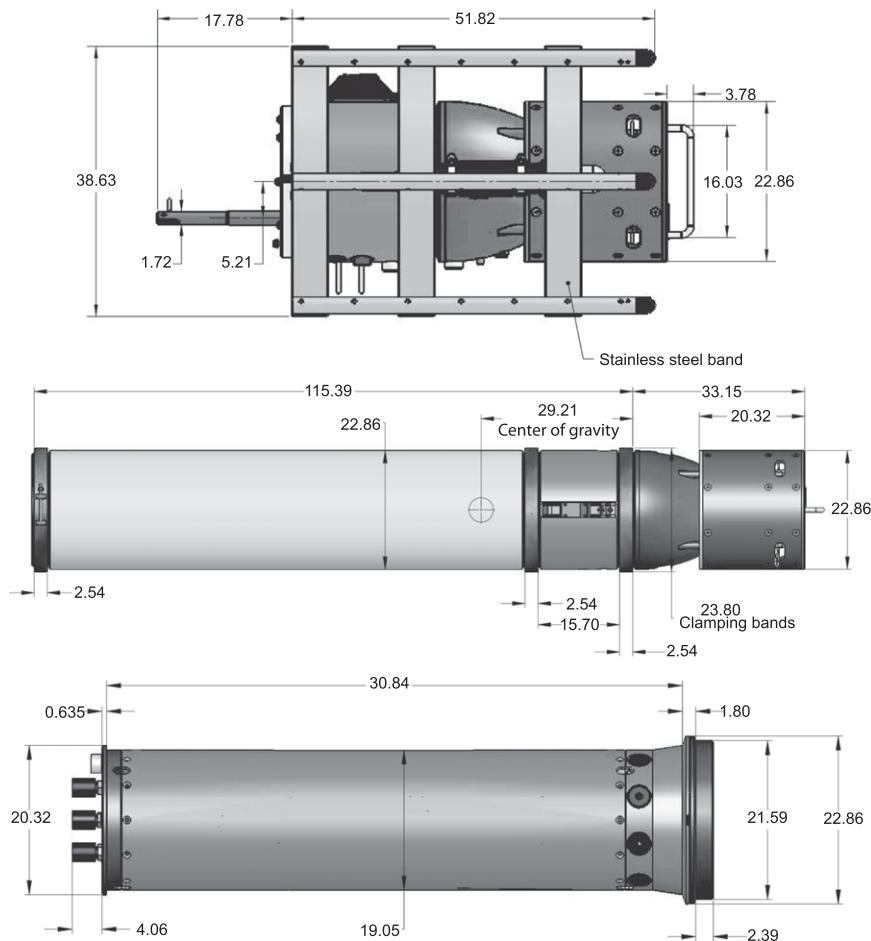


FIG. A2. Principal dimensions of ASIP upon disassembly (cm).

Council co-funded by Marie Curie Actions under FP7. We gratefully appreciate the support from the captain and crew of the R/V *Suroît*, CCGS *Hudson*, R/V *Knorr*, and R/V *Thalassa*. Paula Fratantoni and Jon Hare provided helpful comments for Fig. 8.

APPENDIX A

Mechanical Design

A mechanical drawing of ASIP is shown in Fig. A1 with details of dimensions in Fig. A2. When fully assembled, the instrument has a height of 2.5 m and a weight of 82 kg (in air); this includes a ballast of about 5 kg at the bottom of the instrument. The weight of ASIP in water depends on the water density, and trim weights are attached to allow for a rise velocity of $>0.5 \text{ m s}^{-1}$, which is approximately 1 kg of buoyancy. ASIP profiles vertically upward through the water column, with the sensors located at the top of the instrument in order to minimize wake effects from disturbing the measurements.

The upper section contains a circular guard to provide protection for the sensors (Fig. 12). This guard was based on the Rockland Scientific vertical microstructure profiler 500 (VMP500), whose design was modified to fit ASIP. The guard is made from stainless steel and comes with gussets at its base to provide an attachment point for lines when deploying and recovering. The guard is stiff to prevent mechanical vibration, which would interfere with the microstructure data, which would appear as spikes in the spectra. The four main sections of ASIP are held together with custom-designed V bands that clamp adjoining sections and ensure that the O-rings between sections are adequately compressed; the V bands are tightened with a nut during assembly. The upper section contains all the electronics, and is larger in diameter than the lower section, where ASIP's batteries are located. This design lowers the center of mass and ensures that ASIP is sufficiently stable to remain nearly upright during profiling. There are four stainless guides for the sensor cover (see Fig. 12), which slides into the guides and can be locked in place. The sensor cover is removed immediately prior to deployment.

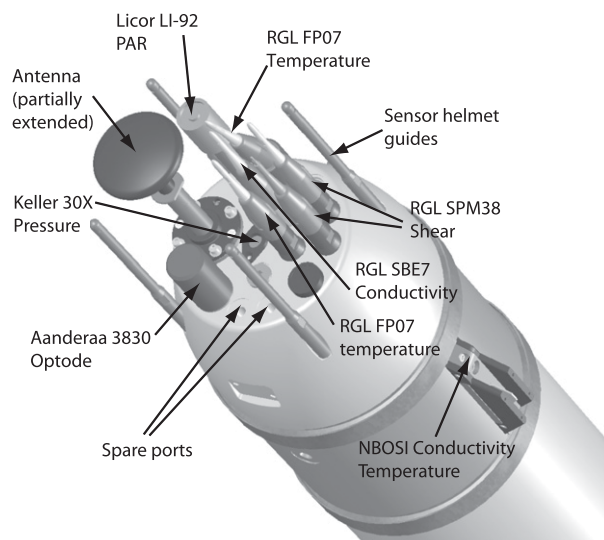


FIG. A3. ASIP sensor endcap.

A detailed view of the sensor endcap is shown in Fig. A3. Sensors come with either digital or analog outputs, so the latter must be converted to digital form. As described in more detail in appendix D, these digital data are assembled with a custom data concentrator board and transmitted to an onboard PC, which we refer to as the Science PC, for storage.

The upper section contains all the remaining circuitry for mission control, data acquisition, communications, and power supply. Location of the analog circuit boards in the upper section minimizes the length of cables to the sensors, thereby reducing pickup noise and other forms of electronic interference. A Novatech ST-400C xenon flasher near the top of the instrument allows ASIP to be sighted at nighttime. This model requires external power, which is provided by ASIP's internal batteries through a SubConn connector. The strobe light has an internal photodiode that prevents it from operating during the daytime, so as to preserve power. During the ascent, the flasher is prevented from firing by a signal from the pressure sensor, to ensure that radio-frequency interference from the strobe will not become embedded in the data stream. Four threaded Swagelok Society of Automotive Engineers (SAE) fittings on the upper section can be removed to provide connectivity to the internal Science PC, where the data are stored, via an Ethernet cable. Communication with the internal mission controller is also provided via an external connector located in the upper section. Details of the mission controller are given in section 4. One of the SAE fittings serves as a marker for an internal reed switch, which is used to provide a wake-up signal to ASIP at deployment time when activated by an external magnet.

The lower section contains six Ultralife UBI-2590 lithium-ion rechargeable battery packs with each pack consisting of two 14.4-V batteries, for a total of 12 individual batteries. These are connected in a two-series/six-parallel configuration, providing a system voltage of 28.8 V. Each battery pack can provide 6 A h, amounting to a total energy of 1036 W h. Based on observed power usage, this amount of energy is estimated to correspond to roughly 6000 m of ascending profiles, although the batteries may be expected to slowly degrade over time. The UBI-2590 battery packs contain a smart battery gauge that can provide battery monitoring information. ASIP's batteries have been configured to allow interrogation of each of the individual batteries, providing information such as battery voltage, current, remaining capacity, and serial number. This configuration was implemented on ASIP to help ensure that the batteries would never become depleted during a deployment, as system power is necessary for satellite communications as well as for operating the xenon flasher. The batteries are rechargeable and an external charger is connected via the ports on the midring (see Fig. A1). Waterproof SAE fittings can be removed to access the electrical connectors, allowing the batteries to be recharged without the need to disassemble ASIP. After hooking up the recharger, the batteries are connected by energizing an internal 24-V relay that then distributes the individual batteries to the recharge connectors. Recharging the batteries from depletion takes about 6 h.

A second guard is attached to the lower shell, and also has several gussets for attachments. The lower guard also supports ASIP vertically in a stable position (e.g., during testing of satellite communications). In addition, it supports three SeaBotix BT-D150 thrusters (see Fig. A1), which are connected to ASIP's endcap with SubConn electrical connectors. These direct current thrusters run at +19 V and are software controlled by the embedded mission computer. Profiling is accomplished by engaging the thrusters, which submerge the instrument to a specified depth. The mission controller, described in more detail below, monitors the pressure during the descent and removes power to the thrusters once the desired depth has been reached. The instrument then ascends through the water column, acquiring data toward the surface.

APPENDIX B

Profiling Modes

The pressure sensor on ASIP is a Keller America 30X, which is flush with the endcap, and provides an accurate record of the depth within the water column. The RS485

TABLE C1. List of commands available for the CF2 ASIP application.

Command	Description
antenna	Extends and retracts the antenna
battery	Communicates with the batteries
help	Displays list of commands
Iridium	Communicates with Iridium modem
minidopp	Communicates with the minidopp 1D profiler
mission	Programs an ASIP mission
pressure	Prints the pressure (decibar)
quit	Reboots to PicoDOS
rev	Displays revision information
science	Communicates with Science PC
thruster	Turns thruster on/off

signal is converted to RS232 and the output is a 3-byte integer in units of pascals ($0\text{--}10^6$). There are also two additional signals: one for overpressure, which causes a relay to latch and removes power from the thruster, and the other to indicate that the surface has been reached and data acquisition should cease.

ASIP can be programmed to operate in either of two different profiling modes: normal and rapid. In the case of the former, ASIP carries out satellite communication (GPS to get a location fix, and Iridium to transmit this information) after every profile, with a specified wait time prior to the next profile. The communications can add several minutes to the profiling operation, so in order to maximize the amount of data acquired in a short deployment period, the rapid profiling mode may be specified. In this mode, ASIP conducts a fixed number of sequential profiles with no surface wait time and without satellite communications, before conducting a single normal profile with these communications.

As a fail-safe, in the event of the mission controller hanging or some other CPU catastrophe, there is a pressure switch that will latch a relay if the depth exceeds 100 m and will prevent power being applied to the thrusters. If this happens, ASIP goes into help mode and continuously transmits an Iridium message containing its status and location.

APPENDIX C

Mission Software and Control

The mission controller on ASIP is a Persistor CF2 microcomputer that runs a C language custom application. Tables C1–C5 refer to aspects of the ASIP application software, as described within this subsection. There is user access to the CF2 RS232 user port via a Teledyne Impulse connector located toward the top of ASIP. This serial connection to a PC allows new versions of the software to

TABLE C2. Parameters required when using the ASIP mission command, e.g., mission 50, 600, 120, 120, 5.

Parameter	Description
Profile depth (m)	Maximum depth to which ASIP descends
Profile delay (s)	Sleep time between profiles
Initial delay (s)	Allows time to get ASIP into the water before beginning the first profile
Total No. of profiles	Maximum number of profiles to be acquired before ASIP quits profiling
No. of rapid profiles	Number of rapid profiles to be conducted between normal profiles

be uploaded to the CF2, as well as sending commands. The available commands are presented in Table C1. An ASIP mission is programmed with the mission command, with the parameters outlined in Table C2. The CF2 then goes into sleep mode, and ASIP is loaded into the small boat and deployed. Once in the water and with the sensor cover removed, the CF2 is woken up by placing an external magnet over a reed switch located in the upper section and marked by one of the SAE fittings. This causes the antenna to extend and a full satellite communication cycle (i.e., GPS and Iridium) is carried out. This message contains the location of the ASIP deployment. After this, an initial countdown occurs (typically 1–2 min) before ASIP starts its first profile. After this delay, the thrusters engage and ASIP descends to a specified depth whereupon the thrusters are powered

TABLE C3. Commands available on the Science PC for controlling the data acquisition. These commands are entered via the user interface on the CF2 mission controller.

Command	Description
\$I	Checks to see if the Science PC is up and running; response is OK
\$TYYMMDDhhmmss	Sets the time on the Science PC, where YY = year (i.e., 09), MM = month, DD = day, hh = hours, mm = minutes, ss = seconds
\$Gmmddhhmm.gnd	Connects the inputs of the AD converter to ground, samples the data for 5 s, and writes to the file mmddhhmm.gnd, where mm = month, dd = day, hh = hour, and mm = minute
\$Cmmddhhmm.cal	Connects the inputs of the AD converter to +2.5 V, samples the data for 5 s, and writes to the file mmddhhmm.cal, where mm = month, dd = day, hh = hour, mm = minute
\$Dmmddhhmm.dat	Samples the analog and digital data for 5 s and writes to the file mmddhhmm.dat, where mm = month, dd = day, hh = hour, mm = minute; this will continue until the \$\$ command is received
\$\$	Stops the data file being sampled
\$Q	Quits the process on the Science PC and shuts it down

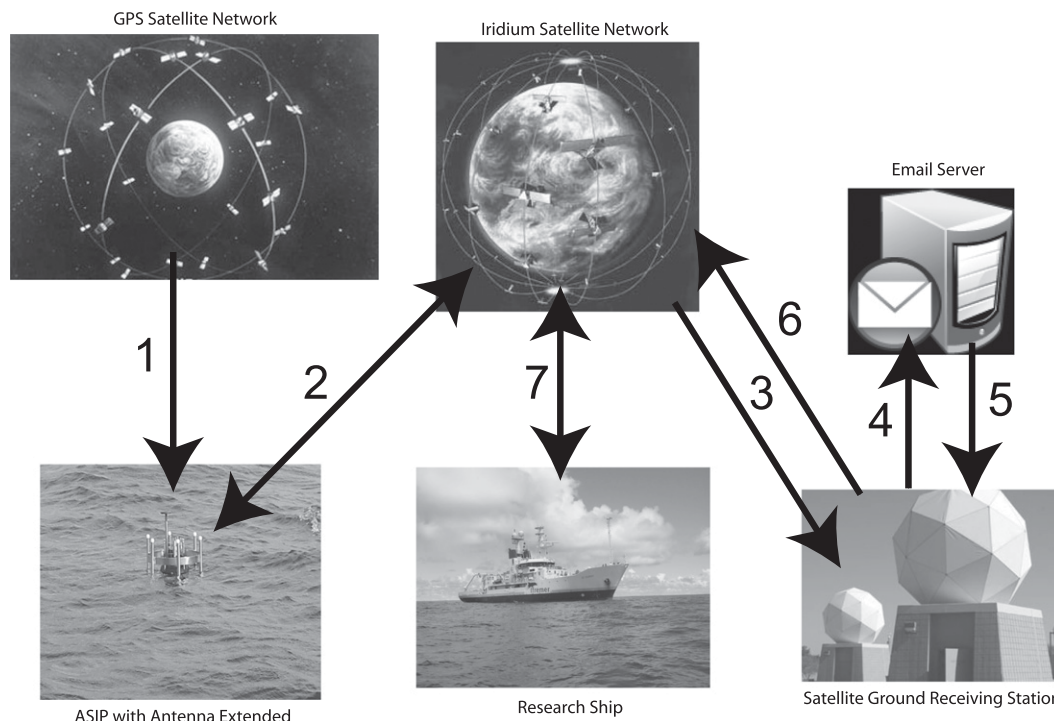


FIG. C1. Description of ASIP message transmission: 1—ASIP receives a GPS location, 2—ASIP transmits the message (see Fig. 15) to the Iridium satellite network using the SBD protocol, 3—this is delivered to an Iridium ground station, 4—the message is delivered as an e-mail attachment, 5—the mail server strips the attachment and retransmits to the Iridium station, 6—this is subsequently transmitted to the satellite, and 7—the message is received on the research ship.

off and ASIP returns to the surface under its own buoyancy. For a normal profile, the CF2 then initiates the communication cycle, described next. After this ASIP goes into a low-power mode until a specified time interval elapses, whereupon the next profile is conducted. The CF2 writes a log of each operation with a time stamp, and this is stored on the compact flash disk.

The output from the data concentrator, described in detail in [appendix D](#), is an 8-bit data stream that is stored on a single-board computer (SBC) running Windows XP (the Science PC). The data and control lines between the Science PC and the concentrator are accomplished with a digital input/output (I/O) card. A dedicated program written in Fortran controls the data flow and storage onto the onboard solid-state hard drive; this program starts automatically when the Science PC is booted. The Science PC gets powered by the mission controller and runs the data handling program—its only task—to acquire and store the data. There is a limited set of commands that may be transmitted to the Science PC from the mission controller over a serial link. These commands are shown in [Table C3](#).

The communication system with ASIP is illustrated in [Fig. C1](#). When at the surface, after a normal profile,

ASIP extends its antenna and attempts to obtain a GPS fix, which will time out after 180 s if a good fix is not obtained. ASIP then transmits a report using the Iridium SBD method with its onboard modem (an NAL Research Corporation model A3LA-PCB-2), with a time-out after five SBD attempts. The report is received at a ground station and forwarded to an e-mail address as

TABLE C4. Commands available for transmission to ASIP from the ship using the Iridium SBD.

Command	Description
DEPTH N	Changes the target depth of the profile to N m
SLEEP N	Changes the sleep interval to N s between profiles
ABORT	Stops profiling and causes ASIP to stay at the surface transmitting a report at an interval specified by HELPSLEEP
EXITHelp	Takes ASIP out of sleep mode and puts it back into profiling mode
HELPSLEEP N	Changes the sleep interval between help transmission to N s
NUMNORM N	Changes the number of normal profiles to N
NUNRAPID N	Changes the number of rapid profiles to N

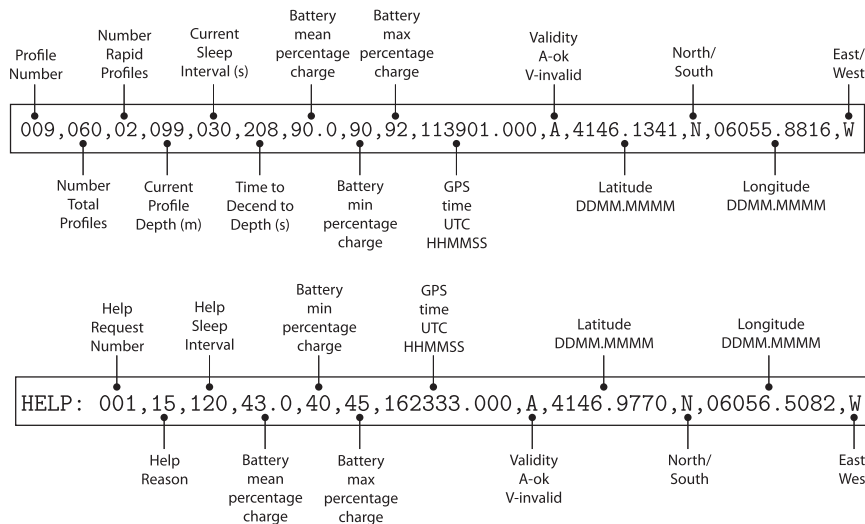


FIG. C2. Explanation of the fields for both the profile and help reports from ASIP.

an attachment. A script running on the mail server strips the attachment and embeds it in another e-mail, which is then delivered to the shipboard modem, again using Iridium SBD. The transmission to reception delay is about 30 s. The Iridium satellite network allows for two-way communication, and so it is possible to change the mission parameters for ASIP by interacting remotely with the mission controller. Messages may be sent to ASIP via the shipboard modem, in the reverse of the pathway by which messages are sent from ASIP to the ship. Table C4 presents the commands that are available to change ASIP's mission parameters during deployment. ASIP will echo back the command via an Iridium message to acknowledge that it has received the command successfully.

There are two types of Iridium messages: profile and help, depending on the current status of ASIP. An example of each is shown in Fig. C2 with an explanation for each field of the message. These messages provide minimal information to the shipboard researchers and provide assurance of correct operation. When ASIP transmits its report in help mode, the reason for going into this mode is transmitted as a numbered code. Table C5 provides a summary of these codes.

APPENDIX D

Data Recording and Format

ASIP has both analog and digital sensors (see Table 1), with the former requiring digitization prior to recording. The analog-to-digital (AD) board consists of four analog devices, AD7765 24-bit, and 112-dB sigma-delta AD converters, operating at a basic conversion

rate of 156-k samples per second. There is an AD motherboard that accommodates four AD boards, providing 16 channels of AD conversion overall. Expansion of the number of AD channels can be easily achieved with additional AD boards. The AD channels can convert voltage or current, programmable with a jumper on the printed circuit boards. To minimize calibration errors associated with temperature fluctuations, the AD circuitry includes an analog switch that clamps each AD input to either 0 or +2.5 V. This feature is controlled by the mission controller, which sends a command to the Science PC (refer to Table C3), which then puts the AD converter boards into one of its three modes: CAL, GND, or DAT, referring to calibration (with the +2.5-V input signal), ground (with the 0-V input signal), or data recording, respectively. Each

TABLE C5. Code number and corresponding reason for going into help mode.

Code	Reason
01	Insufficient resources available to do a profile
02	Received no GPS fix for over 2 h
03	No communications with GPS engine
04	No communications with Iridium modem
05	Unable to transmit Iridium for over 2 h
06	Depth request outside of bounds
07	No response from Science PC (data acquisition)
08	Profile descent time too long
09	Profile ascent time too long
10	Number of specified profiles exceeded
11	"ABORT" command sent over the Iridium
12	Batteries have been depleted to a capacity of less than 20%
13	ASIP has gone below the maximum depth, and pressure switch has been triggered
14	Water leak has been detected
15	Total number of profiles attained

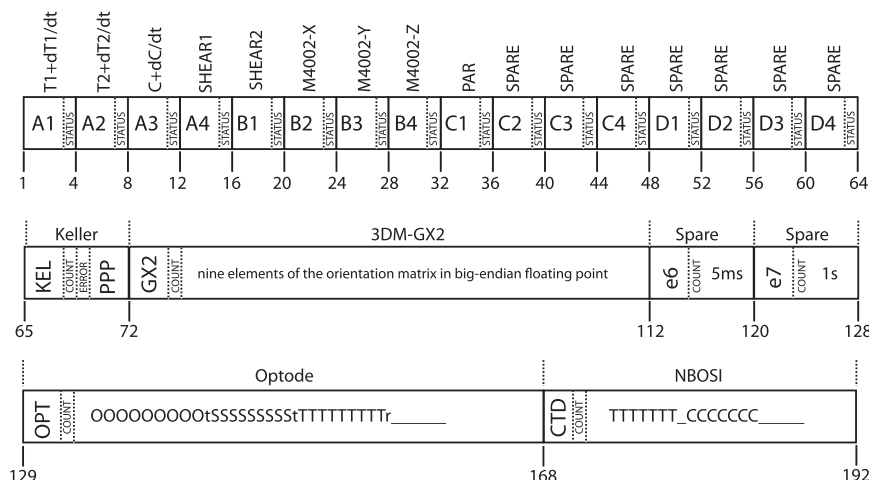


FIG. D1. Format of the ASIP data 192-byte frame.

analog channel is converted into a stream of 4 bytes of data: 3 bytes for the 24-bit digital output, and one status byte (with a value of 0×80 for error-free conversion).

The digital outputs from each sensor are assembled in the data concentrator and logged on the Science PC. A total data frame (i.e., all digital sensors and AD outputs) consists of 192 bytes: sixteen 4-byte AD values (for a total of 64 bytes) followed by 128 bytes of data from the digital sensors, as described in Fig. D1. There are two time counters embedded into the data stream, incrementing at 5-ms and 1-s intervals, respectively. Each of the digital sensors has a marker inserted into the binary data stream, so that the relevant data can be extracted by locating the marker: “KEL” for the 30X Keller pressure sensor, “GX2” for the MicroStrain 3DM-GX2 orientation sensor, “e6” and “e7” for the time counter channels, “OPT” for the Aanderaa oxygen optode sensor, and “CTD” for the NBOSI conductivity–temperature–depth sensor. The data for the Keller pressure sensor consist of 8 bytes: 3 for the KEL marker; 1 byte (termed the COUNT byte) that increments where there is a new value from the sensor (which updates at about 400 Hz); 1 byte to indicate erroneous data; and 3 bytes (PPP) for the absolute value of pressure in units of pascal, with a maximum range for the pressure sensor of about 10^6 Pa or about 100 dB. The digital data for the MicroStrain orientation sensor consumes 40 bytes: 3 for the marker, 1 for the COUNT, and 36 bytes to represent the 3×3 orientation matrix, corresponding to 4 bytes for each of the nine matrix elements. The two spare channels account for 8 bytes: 3 for the time counter markers e6 and e7, and another byte to act as a sequential counter for each frame as a reference for correct decoding. The optode sensor data occupy 40 bytes: 3 for the marker, and 1 for the COUNT, with the remainder

of the 40 bytes containing the ASCII output of the sensor. These ASCII bytes are indicated in Fig. D1, with “O” for oxygen value, “S” for saturation, “T” for temperature, “t” for tab, and “r” for carriage return. Finally, the NBOSI sensor takes up 24 bytes: 3 bytes for the marker, 1 byte for the COUNT, and 20 bytes for the ASCII output of the sensor as indicated in Fig. D1, where “T” is the temperature and “C” is the conductivity.

The sample rate for all channels is precisely 1000.00 Hz, driven by a stable crystal oscillator. However, the digital sensors will output data at their programmed rate. For example, the Keller 30X pressure sensor updates the output at about 400 Hz, while the Aanderaa optode updates its signal at 1 Hz. This scheme was chosen for overall simplicity in data handling. A result is that there are some redundant data, which can be filtered during data processing.

REFERENCES

- Agrawal, Y. C., and A. J. Williams III, 1999: Microstructure sensors dedicated to Dr. Robert W. Stewart, one of the fathers of modern observations of ocean turbulence. *J. Atmos. Oceanic Technol.*, **16**, 1465–1466, doi:[10.1175/1520-0426\(1999\)016<1465:MSDTRD>2.0.CO;2](https://doi.org/10.1175/1520-0426(1999)016<1465:MSDTRD>2.0.CO;2).
- , E. A. Terray, M. A. Donelan, P. A. Hwang, A. J. Williams III, W. M. Drennan, K. K. Kahma, and S. A. Kitaigorodskii, 1992: Enhanced dissipation of kinetic energy beneath surface waves. *Nature*, **359**, 219–220, doi:[10.1038/359219a0](https://doi.org/10.1038/359219a0).
- Anis, A., and J. N. Moum, 1995: Surface wave–turbulence interactions: Scaling $\epsilon(z)$ near the sea surface. *J. Phys. Oceanogr.*, **25**, 2025–2045, doi:[10.1175/1520-0485\(1995\)025<2025:SWISNT>2.0.CO;2](https://doi.org/10.1175/1520-0485(1995)025<2025:SWISNT>2.0.CO;2).
- Bellenger, H., Y. N. Takayabu, T. Ushiyama, and K. Yoneyama, 2010: Role of diurnal warm layers in the diurnal cycle of convection over the tropical Indian Ocean during MISO. *Mon. Wea. Rev.*, **138**, 2426–2433, doi:[10.1175/2010MWR3249.1](https://doi.org/10.1175/2010MWR3249.1).

- Caldwell, D. R., and T. M. Dillon, 1981: An oceanic microstructure measuring system. Oregon State University, School of Oceanography Tech. Rep. 81-10, 168 pp.
- Callaghan, A. H., B. Ward, and J. Vialard, 2014: Influence of surface forcing on near-surface and mixing layer turbulence in the tropical Indian Ocean. *Deep-Sea Res. I*, doi:[10.1016/j.dsr.2014.08.009](https://doi.org/10.1016/j.dsr.2014.08.009), in press.
- Carter, G. D., and J. Imberger, 1986: Vertically rising microstructure profiler. *J. Atmos. Oceanic Technol.*, **3**, 462–471, doi:[10.1175/1520-0426\(1986\)003<0462:VRMP>2.0.CO;2](https://doi.org/10.1175/1520-0426(1986)003<0462:VRMP>2.0.CO;2).
- Dillon, T., J. Richman, C. Hansen, and M. Pearson, 1981: Near-surface turbulence measurements in a lake. *Nature*, **290**, 390–392, doi:[10.1038/290390a0](https://doi.org/10.1038/290390a0).
- Donelan, M. A., B. K. Haus, N. Reul, W. J. Plant, M. Stiassnie, H. C. Graber, O. B. Brown, and E. S. Saltzman, 2004: On the limiting aerodynamic roughness of the ocean in very strong winds. *Geophys. Res. Lett.*, **31**, L18306, doi:[10.1029/2004GL019460](https://doi.org/10.1029/2004GL019460).
- Donlon, C. J., P. J. Minnett, C. Gentemann, T. J. Nightingale, I. J. Barton, B. Ward, and J. Murray, 2002: Towards improved validation of satellite sea surface skin temperature measurements for climate research. *J. Climate*, **15**, 353–369, doi:[10.1175/1520-0442\(2002\)015<0353:TIVOSS>2.0.CO;2](https://doi.org/10.1175/1520-0442(2002)015<0353:TIVOSS>2.0.CO;2).
- Fairall, C. W., E. F. Bradley, J. S. Godfrey, G. A. Wick, J. B. Edson, and G. S. Young, 1996: Cool-skin and warm-layer effects on sea surface temperature. *J. Geophys. Res.*, **101**, 1295–1308, doi:[10.1029/95JC03190](https://doi.org/10.1029/95JC03190).
- Gadgil, S., P. V. Joseph, and N. V. Joshi, 1984: Ocean–atmosphere coupling over monsoon regions. *Nature*, **312**, 141–143, doi:[10.1038/312141a0](https://doi.org/10.1038/312141a0).
- Garau, B., S. Ruiz, W. G. Zhang, A. Pascual, E. Heslop, J. Kerfoot, and J. Tintore, 2011: Thermal lag correction on Slocum CTD glider data. *J. Atmos. Oceanic Technol.*, **28**, 1065–1071, doi:[10.1175/JTECH-D-10-05030.1](https://doi.org/10.1175/JTECH-D-10-05030.1).
- Gentemann, C. L., and P. J. Minnett, 2008: Radiometric measurements of ocean surface thermal variability. *J. Geophys. Res.*, **113**, C08017, doi:[10.1029/2007JC004540](https://doi.org/10.1029/2007JC004540).
- Graham, N. E., and T. P. Barnett, 1987: Sea surface temperature, surface wind divergence, and convection over the tropical oceans. *Science*, **238**, 657–659, doi:[10.1126/science.238.4827.657](https://doi.org/10.1126/science.238.4827.657).
- Gregg, M. C., 1999: Uncertainties and limitations in measuring ϵ and χ_T . *J. Atmos. Oceanic Technol.*, **16**, 1483–1490, doi:[10.1175/1520-0426\(1999\)016<1483:UALIMA>2.0.CO;2](https://doi.org/10.1175/1520-0426(1999)016<1483:UALIMA>2.0.CO;2).
- Hodges, B. A., and D. M. Fratantoni, 2014: AUV observations of the diurnal surface layer in the North Atlantic salinity maximum. *J. Phys. Oceanogr.*, **44**, 1595–1604, doi:[10.1175/JPO-D-13-0140.1](https://doi.org/10.1175/JPO-D-13-0140.1).
- Hu, C., E. T. Montgomery, R. W. Schmitt, and F. E. Muller-Karger, 2004: The dispersal of the Amazon and Orinoco River water in the tropical Atlantic and Caribbean Sea: Observation from space and S-PALACE floats. *Deep-Sea Res.*, **51**, 1151–1171, doi:[10.1016/j.dsr.2004.04.001](https://doi.org/10.1016/j.dsr.2004.04.001).
- Janssen, P. A. E. M., 2012: Ocean wave effects on the daily cycle in SST. *J. Geophys. Res.*, **117**, C00J32, doi:[10.1029/2012JC007943](https://doi.org/10.1029/2012JC007943).
- Kawai, Y., and H. Kawamura, 2002: Evaluation of the diurnal warming of sea surface temperature using satellite-derived marine meteorological data. *J. Oceanogr.*, **58**, 805–814, doi:[10.1023/A:1022867028876](https://doi.org/10.1023/A:1022867028876).
- Kudryavtsev, V., and A. Soloviev, 1990: Slippery near-surface layer of the ocean arising due to daytime solar heating. *J. Phys. Oceanogr.*, **20**, 617–628, doi:[10.1175/1520-0485\(1990\)020<0617:SNSLOT>2.0.CO;2](https://doi.org/10.1175/1520-0485(1990)020<0617:SNSLOT>2.0.CO;2).
- Lorke, A., and F. Peeters, 2006: Toward a unified scaling relation for interfacial fluxes. *J. Phys. Oceanogr.*, **36**, 955–961, doi:[10.1175/JPO2903.1](https://doi.org/10.1175/JPO2903.1).
- Lueck, R. G., F. Wolk, and H. Yamazaki, 2002: Oceanic velocity microstructure measurements in the 20th century. *J. Oceanogr.*, **58**, 153–174, doi:[10.1023/A:1015837020019](https://doi.org/10.1023/A:1015837020019).
- Macoun, P., and R. Lueck, 2004: Modeling the spatial response of the airfoil shear probe using different sized probes. *J. Atmos. Oceanic Technol.*, **21**, 284–297, doi:[10.1175/1520-0426\(2004\)021<0284:MTSROT>2.0.CO;2](https://doi.org/10.1175/1520-0426(2004)021<0284:MTSROT>2.0.CO;2).
- Mammen, T. C., and N. von Bosse, 1990: STEP—A temperature profiler for measuring the oceanic thermal boundary layer at the ocean–air interface. *J. Atmos. Oceanic Technol.*, **7**, 312–322, doi:[10.1175/1520-0426\(1990\)007<0312:STPFMT>2.0.CO;2](https://doi.org/10.1175/1520-0426(1990)007<0312:STPFMT>2.0.CO;2).
- Masson, S., P. Terray, G. Madec, J.-J. Luo, T. Yamagata, and K. Takahashi, 2012: Impact of intra-daily SST variability on ENSO characteristics in a coupled model. *Climate Dyn.*, **39**, 681–707, doi:[10.1007/s00382-011-1247-2](https://doi.org/10.1007/s00382-011-1247-2).
- McManus, M. A., and Coauthors, 2003: Characteristics, distribution and persistence of thin layers over a 48 hour period. *Mar. Ecol. Prog. Ser.*, **261**, 1–19, doi:[10.3354/meps261001](https://doi.org/10.3354/meps261001).
- McNeil, C. L., and L. Merlivat, 1996: The warm oceanic surface layer: Implications for CO₂ fluxes and surface gas measurements. *Geophys. Res. Lett.*, **23**, 3575–3578, doi:[10.1029/96GL03426](https://doi.org/10.1029/96GL03426).
- Minnett, P. J., and B. Ward, 2000: Measurements of near-surface ocean temperature variability—Consequences on the validation of AATSR on ENVISAT. Proc. ERS-ENVISAT Symp., Publ. ESA SP-461, Gothenburg, Sweden, European Space Agency. [Available online at https://earth.esa.int/pub/ESA_DOC/gothenburg/503minne.pdf.]
- , M. Smith, and B. Ward, 2011: Measurements of the oceanic thermal skin effect. *Deep-Sea Res. II*, **58**, 861–868, doi:[10.1016/j.dsr.2.2010.10.024](https://doi.org/10.1016/j.dsr.2.2010.10.024).
- Moum, J. N., M. C. Gregg, R. C. Lien, and M. E. Carr, 1995: Comparison of turbulence kinetic energy dissipation rate estimates from two ocean microstructure profilers. *J. Atmos. Oceanic Technol.*, **12**, 346–366, doi:[10.1175/1520-0426\(1995\)012<0346:COTKED>2.0.CO;2](https://doi.org/10.1175/1520-0426(1995)012<0346:COTKED>2.0.CO;2).
- Oakey, N., and J. Elliott, 1982: Dissipation within the surface mixed layer. *J. Phys. Oceanogr.*, **12**, 171–185, doi:[10.1175/1520-0485\(1982\)012<0171:DWTSML>2.0.CO;2](https://doi.org/10.1175/1520-0485(1982)012<0171:DWTSML>2.0.CO;2).
- Osborn, T. R., and W. R. Crawford, 1980: An airfoil probe for measuring velocity fluctuations in water. *Air-Sea Interaction: Instruments and Methods*, F. Dobson, L. House, and R. Davis, Eds., Plenum Press, 369–386.
- Price, J. F., R. A. Weller, C. M. Bowers, and M. G. Briscoe, 1987: Diurnal response of sea surface temperature observed at the long-term upper ocean study (34°N, 70°W) in the Sargasso Sea. *J. Geophys. Res.*, **92**, 14 480–14 490, doi:[10.1029/JC092iC13p14480](https://doi.org/10.1029/JC092iC13p14480).
- Reul, N., J. Tenerelli, J. Boutin, B. Chapron, F. Paul, E. Brion, F. Gaillard, and O. Archer, 2012: Overview of the first SMOS sea surface salinity products. Part I: Quality assessment for the second half of 2010. *IEEE Trans. Geosci. Remote Sens.*, **50**, 1636–1647, doi:[10.1109/TGRS.2012.2188408](https://doi.org/10.1109/TGRS.2012.2188408).
- Reverdin, G., S. Morisset, J. Boutin, and N. Martin, 2012: Rain-induced variability of near sea-surface T and S from drifter data. *J. Geophys. Res.*, **117**, C02032, doi:[10.1029/2011JC007549](https://doi.org/10.1029/2011JC007549).
- Roemmich, D., and W. Owens, 2000: The Argo project: Global ocean observations for understanding and prediction of

- climate variability. *Oceanography*, **13**, 45–50, doi:[10.5670/oceanog.2000.33](https://doi.org/10.5670/oceanog.2000.33).
- Soloviev, A. V., and P. Schlüssel, 1996: Evolution of cool skin and direct air–sea gas transfer coefficient during daytime. *Bound.-Layer Meteor.*, **77**, 45–68, doi:[10.1007/BF00121858](https://doi.org/10.1007/BF00121858).
- , and R. Lukas, 1997: Observation of large diurnal warming events in the near-surface layer of the western equatorial Pacific warm pool. *Deep-Sea Res. I*, **44**, 1055–1076, doi:[10.1016/S0967-0637\(96\)00124-0](https://doi.org/10.1016/S0967-0637(96)00124-0).
- , N. V. Vershinsky, and V. A. Bezverchnii, 1988: Small-scale turbulence measurements in the thin surface layer of the ocean. *Deep-Sea Res.*, **35A**, 1859–1874, doi:[10.1016/0198-0149\(88\)90113-6](https://doi.org/10.1016/0198-0149(88)90113-6).
- Stevens, C., and M. Smith, 2004: Temperature microstructure beneath surface gravity waves. *J. Atmos. Oceanic Technol.*, **21**, 1747–1757, doi:[10.1175/JTECH1659.1](https://doi.org/10.1175/JTECH1659.1).
- Stewart, R. W., 1974: The air–sea momentum exchange. *Bound.-Layer Meteor.*, **6**, 151–167, doi:[10.1007/BF00232481](https://doi.org/10.1007/BF00232481).
- Sutherland, G., K. H. Christensen, and B. Ward, 2013: Wave-turbulence scaling in the ocean mixed layer. *Ocean Sci.*, **9**, 597–608, doi:[10.5194/os-9-597-2013](https://doi.org/10.5194/os-9-597-2013).
- , —, and —, 2014: Evaluating Langmuir turbulence parameterizations in the ocean surface boundary layer. *J. Geophys. Res. Oceans*, **119**, 1899–1910, doi:[10.1002/2013JC009537](https://doi.org/10.1002/2013JC009537).
- Sweeney, C., A. Gnanadesikan, S. M. Griffies, M. J. Harrison, A. J. Rosati, and B. L. Samuels, 2005: Impacts of shortwave penetration depth on large-scale ocean circulation and heat transport. *J. Phys. Oceanogr.*, **35**, 1103–1119, doi:[10.1175/JPO2740.1](https://doi.org/10.1175/JPO2740.1).
- Thorpe, S. A., 2004: Recent developments in the study of ocean turbulence. *Annu. Rev. Earth Planet. Sci.*, **32**, 91–109, doi:[10.1146/annurev.earth.32.071603.152635](https://doi.org/10.1146/annurev.earth.32.071603.152635).
- Vialard, J., and Coauthors, 2009: Cirene: Air–sea interactions in the Seychelles–Chagos thermocline ridge region. *Bull. Amer. Meteor. Soc.*, **90**, 45–61, doi:[10.1175/2008BAMS2499.1](https://doi.org/10.1175/2008BAMS2499.1).
- Wang, Z., and L. Goodman, 2009: The evolution of a thin phytoplankton layer in strong turbulence. *Cont. Shelf Res.*, **30**, 104–118, doi:[10.1016/j.csr.2009.08.006](https://doi.org/10.1016/j.csr.2009.08.006).
- Wanninkhof, R., W. E. Asher, D. T. Ho, C. Sweeney, and W. R. McGillis, 2009: Advances in quantifying air–sea gas exchange and environmental forcing. *Annu. Rev. Mar. Sci.*, **1**, 213–244, doi:[10.1146/annurev.marine.010908.163742](https://doi.org/10.1146/annurev.marine.010908.163742).
- Ward, B., 2006: Near-surface ocean temperature. *J. Geophys. Res.*, **111**, C02005, doi:[10.1029/2004JC002689](https://doi.org/10.1029/2004JC002689).
- , R. Wanninkhof, P. J. Minnett, and M. J. Head, 2004: SkinDeEP: A profiling instrument for upper-decameter sea surface measurements. *J. Atmos. Oceanic Technol.*, **21**, 207–222, doi:[10.1175/1520-0426\(2004\)021<0207:SAPIFU>2.0.CO;2](https://doi.org/10.1175/1520-0426(2004)021<0207:SAPIFU>2.0.CO;2).
- Webster, P. J., C. A. Clayson, and J. A. Curry, 1996: Clouds, radiation, and the diurnal cycle of sea surface temperature in the tropical western Pacific. *J. Climate*, **9**, 1712–1730, doi:[10.1175/1520-0442\(1996\)009<1712:CRATDC>2.0.CO;2](https://doi.org/10.1175/1520-0442(1996)009<1712:CRATDC>2.0.CO;2).
- Yamazaki, H., and T. R. Osborn, 1990: Dissipation estimates for stratified turbulence. *J. Geophys. Res.*, **95**, 9739–9744, doi:[10.1029/JC095iC06p09739](https://doi.org/10.1029/JC095iC06p09739).
- Zappa, C. J., W. R. McGillis, P. A. Raymond, J. B. Edson, E. J. Hints, H. J. Zemelink, J. W. H. Dacey, and D. T. Ho, 2007: Environmental turbulent mixing controls on air–water gas exchange in marine and aquatic systems. *Geophys. Res. Lett.*, **34**, L10601, doi:[10.1029/2006GL028790](https://doi.org/10.1029/2006GL028790).
- Zhang, Y., and X. Zhang, 2012: Ocean haline skin layer and turbulent surface convections. *J. Geophys. Res.*, **117**, C04017, doi:[10.1029/2011JC007464](https://doi.org/10.1029/2011JC007464).